Large-scale galaxy distribution in the Las Campanas Redshift Survey

A. G. Doroshkevich,[1,2]★ D. L. Tucker,[3] R. Fong,[4] V. Turchaninov[2] and H. Lin[5]

[1]*Theoretical Astrophysics Center, Juliane Maries Vej 30, DK-2100 Copenhagen Ø, Denmark*
[2]*Keldysh Institute of Applied Mathematics, Russian Academy of Sciences, 125047 Moscow, Russia*
[3]*Fermi National Accelerator Laboratory, MS 127, PO Box 500, Batavia, IL 60510, USA*
[4]*Department of Physics, University of Durham, Durham DH1 3LE*
[5]*Steward Observatory, University of Arizona, 933 N. Cherry Avenue, Tucson, AZ 85721, USA*

ABSTRACT

We make use of three-dimensional clustering analysis, inertia tensor methods, and the minimal spanning tree technique to estimate some physical and statistical characteristics of the large-scale galaxy distribution and, in particular, of the sample of overdense regions seen in the Las Campanas Redshift Survey (LCRS). Our investigation provides additional evidence for a network of structures found in our core sampling analysis of the LCRS: a system of rich sheet-like structures, which in turn surround large underdense regions crisscrossed by a variety of filamentary structures.

We find that the overdense regions contain ~40–50 per cent of LCRS galaxies and have proper sizes similar to those of nearby superclusters. The formation of such structures can be roughly described as a non-linear compression of protowalls of typical cross-sectional size ~ 20–$25\,h^{-1}$ Mpc; this scale is ~5 times the conventional value for the onset of non-linear clustering – to wit, r_0, the autocorrelation length for galaxies.

The comparison with available simulations and theoretical estimates shows that the formation of structure elements with parameters similar to those observed is presently possible only in low-density cosmological models, $\Omega_m h \sim 0.2$–0.3, with a suitable large-scale bias between galaxies and dark matter.

Key words: surveys – galaxies: clusters: general – large-scale structure of Universe.

1 INTRODUCTION

The existence in the local Universe of structures as large as ~ 50–$100\,h^{-1}$ Mpc ($h \equiv H_0/100\,{\rm km\,s^{-1}\,Mpc^{-1}}$) has been one of the most intriguing problems of modern cosmology. The pioneering studies of such structures include those of Oort (1983a,b), who outlined the nearby superclusters; Kirshner et al. (1983), who found the Great Void in Boötes; Dressler et al. (1987), who discovered the Great Attractor; de Lapparent, Geller & Huchra (1988), who outlined the Great Wall; and Bahcall (1988), who studied the clustering of rich clusters. The problem became even more intriguing with the announcement of an unexpectedly very-large-scale, $\sim 120\,h^{-1}$ Mpc, quasi-periodic modulation in the spatial galaxy distribution in the galaxy catalogue analysed by Broadhurst et al. (1990). Although some of these discoveries have proven controversial – and the apparent regularity of the latter was eventually shown to be an artefact of the observations (see, for example, Ramella, Geller & Huchra 1992) – they clearly gave impetus to the study of the local Universe on ever larger scales.

Indeed, the past few years have seen great advances in the

observational data available for the detailed study of structure on such large scales. In particular, with the advent of such large redshift surveys as the Durham/UKST Galaxy Redshift Survey (DURS) (Ratcliffe et al. 1996) and the Las Campanas Redshift Survey (LCRS) (Shectman et al. 1996), we can now begin a fruitful exploration of structure on scales of up to $\sim 300\,h^{-1}$ Mpc. Such studies act as forerunners to the enormous scientific potential of the huge observational data sets of the near future, such as those of the 250 000-galaxy 2dF Redshift Survey (Colless 1999) and the 1 000 000-galaxy Sloan Digital Sky Survey (Loveday & Pier 1998).

This paper specifically addresses the LCRS. In an earlier work with the LCRS sample (Doroshkevich et al. 1996; hereafter Paper I), we used the one-dimensional (1D) core-sampling technique developed by Buryak, Doroshkevich & Fong (1994). Therein, we found a sample of overdense regions surrounding huge (50–$70\,h^{-1}$ Mpc) underdense regions or 'voids' (as they have been termed in the literature). The sample of overdense regions is composed of rich wall-like structures (containing ~50 per cent of LCRS galaxies), whereas the underdense regions are criss-crossed by filaments having a variety of richnesses. Evidence for a sample of overdense regions had been seen before – both in the LCRS

★ E-mail: dorr@tac.dk

(Landy et al. 1996; Tucker et al. 1997) and in various deep pencil-beam surveys (Broadhurst et al. 1990; Buryak et al. 1994; Willmer et al. 1994; Bellanger & de Lapparent 1995; Cohen et al. 1996). Previous wide-angle surveys, however, have been hampered in their investigations of the overdense regions owing to their relative lack of depth; e.g. the well-known CfA (de Lapparent et al. 1988) and SSRS (da Costa et al. 1988) surveys are limited to depths of ~ 100–$150\,h^{-1}$ Mpc and include at most one wall-like structure. In fact, owing to its relative depth, the LCRS is the first wide-angle survey in which a representative sample of walls and 'voids' could be extracted.

Our previous statistical estimates of the properties and parameters of the large-scale galaxy distribution, based upon core-sampling analysis of the LCRS, have shown that the richer walls are similar to the Great Wall (de Lapparent et al. 1988; Ramella et al. 1992) and nearby superclusters of galaxies (Oort 1983); they are the largest structures seen in the observed galaxy distribution. Unfortunately for the ease of automated identification, these walls are significantly disrupted by the small-scale clustering of galaxies – for example, the Great Wall itself is composed of a variety of dense clumps and filaments that are clearly seen in fig. 5 of Ramella et al. (1992). In the LCRS this disruption is enhanced by field-to-field sampling effects and by the relatively small angular size of fields ($1°\!.5$), and, therefore, the walls in the LCRS appear as a set of highly dense clusters linked by lower-density bridges. Even so, these walls are relatively high-contrast features in comparison with their surroundings, and this fact greatly aids in their identification and subsequent analysis. The first example of the identification of individual walls based upon the LCRS was presented in Doroshkevich et al. (1998).

Furthermore, the structures within the underdense regions are also of interest. Core-sampling has shown that the filaments which fill the gaps between the walls are connected in a random network or, more accurately, in a random *broken* network. Although not as striking as the 'Great Walls' making up the sample of overdense regions, they are far more common a structure and contain perhaps up to ~ 50 per cent of all LCRS galaxies. Unfortunately, the combination of their broken structure, their meandering paths, and their many-branched shapes makes the identification and characterization of these filamentary structures a difficult task. None the less, some statistical characteristics of these filaments can be measured, as we will describe later. For that, and for the analysis of individual walls and filaments, complementary three-dimensional (3D) methods must be employed.

In this paper three such methods are used. One is a standard 'friends-of-friends' clustering analysis, which permits the extraction of individual structure elements from the point distribution under consideration. This technique is supplemented by inertia tensor analysis (see, for example, Vishniac 1986), which allows us to estimate the lengths, widths and thicknesses of clusters directly. Of course, clusters so defined depend on the linking length used. The interesting statistics are then the variations of cluster properties with the linking length. The third method is that of the minimal spanning tree (MST) technique (Barrow, Bhavsar & Sonoda 1985; van de Weygaert 1991). Some applications of the MST technique can be found in Bhavsar & Ling (1988) and in Martinez et al. (1990). Here it is employed for the more detailed description of the general galaxy distribution, and of the inner structure of the richer clusters making up the overdense regions and the inner structure of the underdense regions. Additionally, the MST analysis is also the logical technique for the simultaneous extraction of the set of all cluster catalogues for a very wide range in linking lengths for use in the two previous methods of analysis.

We do, however, note this caveat of our analyses: the LCRS was not planned with clustering and MST analyses in mind. In some senses, it is not truly a 3D survey, owing to the relatively small angular size of the field of observation ($1°\!.5 \times 1°\!.5$). The comparison of results obtained from the LCRS, from the DURS, and from simulations shows the influence of this factor. Nevertheless, on account of its relative depth and number of galaxies, the LCRS is the best wide-field redshift survey presently available for our analyses. Together with the similar study of DURS and of N-body simulations, these analyses of LCRS provide a good first estimate of some of the physical parameters of the large-scale structure in the Universe and, perhaps more importantly, show the promise these methods hold for analysing the 2dF Galaxy Redshift Survey and Sloan Digital Sky Survey.

Thus, we find that the statistical estimates made here of the physical parameters of structure elements can indeed be directly compared with theoretical predictions (Demiański & Doroshkevich 1999a,b) and with the results obtained using these same techniques from the DURS (Doroshkevich et al. 2000), from simulated dark matter distributions (Doroshkevich et al. 1999, hereafter DMRT), and from the mock catalogues prepared by Cole et al. (1998; hereafter CHWF). The comparison allows us to analyse the influence of the peculiar selection effects inherent to the LCRS and, in particular, to discriminate cosmological models that yield structures like those found within this survey. Additionally, a more detailed comparison of these results with those from simulated mock catalogues can provide a test of bias models used for extracting 'galaxy' catalogues from simulations; such a comparison may also be used to connect characteristics of the richer wall-like condensations with basic cosmological parameters and with the initial perturbation spectrum. These topics will be considered in future papers.

The present paper is organized as follows. First, the analysis techniques are introduced in Section 2. Next, the general properties of the LCRS galaxy distribution are characterized in Section 3. Then, subsamples of structure elements are extracted and analysed in Section 4, and the properties of the richer clusters that make up the overdense regions are discussed in Section 5. Some characteristics of the filamentary component of structure that lie mostly in the underdense regions are found in Section 6. Finally, the results of our investigations are summarized and discussed in Section 7.

2 CLUSTERING ANALYSIS AND THE MINIMAL SPANNING TREE TECHNIQUE

In this paper we use both the statistics of separate clusters (supplemented by the inertia tensor method) and a more general description of the galaxy distribution given by the variation of the number of clusters $N_{cl}(r_{link})$ versus linking length r_{link} (the NCLL method). The former provides us with the standard quantitative characteristics of richer structure elements, and the latter characterizes the relative distribution of – and the links among – the individual clusters and galaxies.

For a more detailed characteristic of the 'general network' of galaxies, the MST technique is also used. The MST is a construct from graph theory, originally introduced by Kruskal (1956) and Prim (1957), which has been widely applied in telecommunications and similar fields. It is a 'unique network' associated with a given point sample and connects all points of the sample to a 'tree'

in a special and unique manner that minimizes the full length of the tree. One of its earliest uses in the study of large-scale structure was that of Bhavsar & Ling (1988), who successfully applied it to extract filamentary structures from the original CfA Redshift Survey. Further definitions, examples, and applications of this approach are discussed in Barrow et al. (1985) and van de Weygaert (1991). More references to the mathematical results can also be found in van de Weygaert (1991). Here we will restrict our investigation to our results for the 'probability distribution function of the MST edge lengths' $W_{MST}(l)$ (the PDF MST method) and to the morphological description of individual clusters. The potential of the MST approach is not, however, exhausted by these applications.

The PDF MST method and the NCLL method are related in that the set of clusters for a given linking length in the NCLL method is extracted by the process of 'separating' the MST of the galaxy distribution – i.e. removing any edges from the MST with length that exceeds that linking length. Basically, the MST for a galaxy distribution contains within it all 'friends-of-friends' cluster catalogues for all linking lengths; if the MST is separated for a given linking length, one then has the 'friends-of-friends' cluster catalogue for that linking length. This is one of the many strengths of MSTs.

As we will see, both the NCLL and the PDF MST techniques can be used to examine the geometry of a galaxy distribution. In the general case both $N_{cl}(r_{link})$ and $W_{MST}(l)$ depend on the correlation functions (or cumulants) of all orders. For larger point separations, however, where some correlations become small and the cumulants tend to constants, the appearance of a Poisson-like point distribution can be expected (White 1979; Buryak, Demiański & Doroshkevich 1991; Sahni & Coles 1995; Borgani 1996). In such a case both the NCLL and the PDF MST techniques can characterize the geometry of a point distribution.

For example, consider a random point distribution situated along randomly distributed straight lines and flat planes. Even for such a distribution of points, correlations do not vanish in 3D space and for the suitable set of such lines and planes the two-point correlation function is consistent with the observed power law, $\xi(r) \propto r^{-1.8}$ (Buryak & Doroshkevich 1996). The NCLL and PDF MST techniques are able to reveal the geometry of such a point distribution.

2.1 The NCLL method

Three-dimensional clustering analysis (the 'friends-of-friends' cluster-finding method) is well known (see, for example, Sahni & Coles 1995). Hence, the main relationships are listed here without proof simply in order to introduce the notation.

To characterize a sample of galaxies quantitatively, the total number of clusters versus the linking length can be fitted for both small and large values of b to the parametric expression

$$N_{cl}(r_{link}) = N_{gal}\exp(-\alpha_{cl}b^{p_{cl}}), \tag{2.1}$$

$$b \equiv \left(\frac{4\pi}{3}\langle n_{gal}^{obs}\rangle r_{link}^3\right)^{1/3},$$

where b is a standard dimensionless linking length and N_{gal} and $\langle n_{gal}^{obs}\rangle$ are the number of galaxies and the mean 3D number density of galaxies in the sample, respectively.

The parameter b characterizes the *local* threshold density bounding the cluster. Indeed, the definition of a cluster implies that for each particle there is at least one neighbour at the distance

$r \lesssim r_{link}$ while other particles lie at distances $r > r_{link}$ from the cluster boundary. This means that the local threshold density bounding the cluster can be written as

$$n_{thr} \gtrsim \left(\frac{4\pi}{3}r_{link}^3\right)^{-1} = b^{-3}\langle n_{gal}^{obs}\rangle.$$

The coefficient α_{cl} in relation (2.1) characterizes the number density of the point distribution.

The interpretation of the power index p_{cl}, however, is more complicated. However, very nicely, for the simple case of either a one- or two-dimensional (2D) Poisson point distribution this index is identical to the space dimension of the distribution (Kendall & Moran 1963; White 1979; Buryak et al. 1991; Sahni & Coles 1995; Borgani 1996). Hence, when these indices are close to 1 or 2 for some range of b, the function $N_{cl}(r_{link})$ is close to that for a 1D or 2D Poisson distribution and it is expected that filaments or walls dominate the point population, i.e. when $p_{cl} \approx 1$ or 2, respectively. It will be shown below that, for all samples under investigation, such cases are realized for larger b.

Although the interpretation of the power index p_{cl} as an 'effective dimension' of the galaxy distribution is useful, it is not obligatory. It does not mean that galaxies are necessarily distributed along a line (or sheet) even if $p_{cl}(b)$ is a weak function of b, but rather that random points distributed along a system of identical lines and/or sheets would reproduce the same functional form for $N_{cl}(r_{link})$. However, it can provide a quantitative corroboration of the visual observation of a distribution as apparently dominated by filaments or walls.

Note that the application of the NCLL method is restricted by the onset of percolation. The formation of a very big – in the limiting case, infinite – cluster occurs for the critical linking length, $r_{link} = r_{perc}$, leading to a rapid drop in the number of clusters at larger linking lengths.

In practice, however, rather than using relation (2.1), it is more convenient to use a five-parameter fit,

$$N_{cl}(b) = N_{gal}\exp(-F_{cl}), \quad F_{cl} \equiv (\beta_1 b^{p_1} + \beta_2 b^{p_2})^{p_3},$$

$$p_{cl}(b) = \frac{d\ln(F)}{d\ln b} = p_3\frac{p_1\beta_1 b^{p_1} + p_2\beta_2 b^{p_2}}{\beta_1 b^{p_1} + \beta_2 b^{p_2}}, \tag{2.2}$$

which permits a continuous description of the variation of $p(b)$ over a wide range in b. For both small and large values of b, this fit approaches that of relation (2.1).

This fit has been tested with one-, two- and three-dimensional simulated random point distributions and the expected theoretical expressions has been reproduced up to the onset of percolation.

2.2 The PDF MST method

To obtain the quantitative description of the PDF MST for both small and large values of the edge length l, a three-parameter fit can be applied:

$$W_{MST}(l) = W_0 x^{p_{MST}-1}\exp(-\alpha_{MST}x^{p_{MST}}), \tag{2.3}$$

$$x = \frac{l}{\langle l_{MST}\rangle}, \quad b_{MST} = \left(\frac{4\pi}{3}\langle n_{gal}^{obs}\rangle\right)^{1/3}\langle l_{MST}\rangle,$$

where $\langle l_{MST}\rangle$ is the mean edge length, p_{MST} and α_{MST} are the dimensionless fitting parameters and the value W_0 serves as the normalization of the PDF MST. This relation is consistent with that of relation (2.1) because the number of clusters is actually the

cumulative PDF for the MST edges, i.e.

$$N_{\mathrm{cl}}(r_{\mathrm{link}}) \propto \int_{r_{\mathrm{link}}}^{\infty} W_{\mathrm{MST}}(l)\, \mathrm{d}l.$$

Furthermore, as with their NCLL counterparts, the parameters α_{MST} and p_{MST} are also linked, respectively, with the observed number density of points in the sample under investigation and, for a Poisson point distribution, with the space dimension of the dominant structures.

For richer samples a six-parameter fit similar to relation (2.2) can be used as well. In this case the PDF MST is fitted to the relationship

$$W_{\mathrm{MST}}(l) = W_0 \frac{\mathrm{d}F_{\mathrm{MST}}}{\mathrm{d}x} e^{-F_{\mathrm{MST}}}, \quad x = \frac{l}{\langle l_{\mathrm{MST}} \rangle}, \qquad (2.4)$$

where the corresponding definitions from relation (2.2) for the function $F(x)$ and the power index $p(x)$ are used. This fit allows us to trace the variation of $p(x)$ with l and to discriminate roughly between regions where $p(x) \rightarrow$ constant. and the PDF MST under consideration becomes Poisson-like.

As with relation (2.2), this fit has also been tested with simulated random point distributions and the expected theoretical expressions have been reproduced up to the onset of percolation. For a 3D Poisson point distribution percolation can clearly be seen in the shape of the PDF MST as a drastic cut-off at $l \approx l_{\mathrm{perc}}$. In all cases the power indices $p_{\mathrm{MST}} \approx p_{\mathrm{cl}}$ were found to be identical to the space dimension of the distribution.

2.3 The inertia tensor method

Cluster sizes can be estimated with the inertia tensor method (Vishniac 1986; Babul & Starkman 1992). The inertia tensor, I_{ij}, for each cluster can be written as

$$I_{ij} = \frac{5}{N_{\mathrm{mem}}} \sum_{N_{\mathrm{mem}}} [q_i - q_i^{(0)}][q_j - q_j^{(0)}], \qquad (2.5)$$

where q_i and $q_i^{(0)}$ are the respective coordinates of the particles and of the centre of mass of the cluster, N_{mem} is the number of particles in the cluster, and the conventional normalization 5 has been chosen in order to be consistent with a homogeneous ellipsoid. Hence, the principal values of the tensor I_{ij}, namely the length (diameter) L, the width w, and the thickness t ($L \geqslant w \geqslant t$), give us an objective estimate of a cluster's size and volume,

$$V = \frac{\pi}{6} Lwt. \qquad (2.6)$$

Naturally, it is a somewhat arbitrary and limited estimate of the true cluster volume, and its advantages and disadvantages are well known (see, for example, Sathyaprakash, Sahni & Shandarin 1998). Clearly, the accuracy of this approach is higher for compact regular clusters (those which can be approximated by a convex ellipsoid) and the final estimates depend heavily on the cluster shape, curvature and number of branches of the MST spanning the cluster. This is caused by the random variation in cluster shapes and by the integration of separate elements into the joint network. Thus, for example, results for a cluster formed by the intersection of two filaments or by a very curved filament will be far from the true values. These estimates are also quite sensitive to the arrangement of highly dense substructures within the structure elements. In practice, the impact of random factors gives rise to an artificial growth of the measured width and thickness of the cluster

and results in axial ratios of $\langle w/L \rangle \approx \langle t/w \rangle \sim 0.5 \pm 0.2$, which are typical for amorphous elliptical aggregates. It is a direct consequence of describing a cluster by a convex ellipsoid in the inertia tensor method. Nevertheless, for all its drawbacks, it is a simple descriptor of the cluster size; below, we will restrict our analysis to the estimates of the parameters L, w and t.

2.4 The morphology of the structure elements through the MST characteristics

Another measure of cluster morphology is based upon building an MST for each cluster individually and then characterizing the morphology of the structure element by the ratio $L_{\mathrm{tr}}/L_{\mathrm{sum}}$, where L_{sum} and L_{tr} are, respectively, the full length of the MST edges and the length of the trunk that is the maximal path of the tree. It can be expected that even for curved filaments the trunk will be a dominant part of the tree and, therefore, $L_{\mathrm{tr}}/L_{\mathrm{sum}} \sim 1$. The presence of high-density substructures and/or short branches cannot substantially increase L_{sum} owing to the small edge lengths typical for such cores. However, the presence of longer branches decreases $L_{\mathrm{tr}}/L_{\mathrm{sum}}$ even for relatively poor clusters. Such trees are more typical for sheet-like elements and/or irregular elliptical clouds for which the ratio $L_{\mathrm{tr}}/L_{\mathrm{sum}} \leqslant 0.5$ is much more probable. Hence, this approach can discriminate among the simple filamentary-like structure elements, but more refined methods are required to characterize richer sheet-like structure elements. The morphology of very rich clusters or of the set of such clusters can also be characterized with the PDF MST technique described in Section 2.2 (see Section 5.4 below).

3 THE GALAXY DISTRIBUTION IN THE LCRS

3.1 The LCRS sample

The LCRS is organized as a set of six slices, three of which – the LCRS-1 ($\delta = -3°$), LCRS-2 ($\delta = -6°$) and LCRS-3 ($\delta = -12°$) – are located towards the Northern Galactic Cap, and three of which – the LCRS-4 ($\delta = -39°$), LCRS-5 ($\delta = -42°$) and LCRS-6 ($\delta = -45°$) – are located towards the Southern Galactic Cap. Each slice consists of a set of fields of angular size $1°.5 \times 1°.5$.

The LCRS used a fibre-fed multi-object spectrograph (MOS) to obtain its galaxy redshifts. One part of the survey (≈ 80 per cent of the galaxies) was performed with 112 fibres in each field and includes galaxies within a nominal apparent magnitude range of $15.0 < m_R \leqslant 17.7$, but the other, earlier part (≈ 20 per cent of galaxies) was performed with 50 fibres in each field and includes galaxies within a nominal range of $16.0 < m_R \leqslant 17.3$. For observing efficiency, all the fibres were used, but each field was observed only once. If, as was typically the case, there were more galaxies within the magnitude limits than there were fibres, a random subsample of galaxies was targeted by fibres; if there were too few galaxies, the range in the nominal magnitude limits was increased until the number of galaxies equalled the number of fibres.

Such an observing strategy resulted in two competing sampling effects. The stronger of these two effects was that the number of galaxies in a 112-fibre field was roughly twice that in a 50-fibre field, yielding factor-of-2 artificial inhomogeneities in the apparent galaxy distribution. This effect is most noticeable in the three southern slices (LCRS-4, LCRS-5 and LCRS-6), in which 50- and

112-fibre fields alternate across a slice, lending the apparent galaxy distribution in these slices a slightly 'picket-fence' appearance.

On the other hand, the random culling of galaxies to fit the number of targets to the number of available fibres in a given field tends to homogenize the apparent galaxy distribution: extremely rich regions of the sky are undersampled relative to poorer regions. This competing second effect, however, is small by comparison – rms variations in the field-to-field random sampling range from about 20 per cent for the 112-fibre fields to about 30 per cent for the 50-fibre fields.

The combination of these two selection effects results in an overall 'field-to-field sampling variation effect' which needs to be taken into account in our analyses. Clearly, we are more concerned with the larger contributor to this effect – the intermixture of 50- and 112-fibre fields. Fortunately, slice LCRS-3 includes only 112-fibre fields and slice LCRS-2 is composed almost entirely of 50-fibre fields (and merely four 112-fibre fields); the comparison between these two slices allows us to estimate the possible influence of sampling effects on our results. For other slices the two types of field are intermixed, which tends to disrupt the regular character of the observed structures. Furthermore, on average, an intermixed slice contains only about 80 per cent of the number of galaxies of the one slice made up entirely of 112-fibre fields.

Another peculiarity of the LCRS is a slight depression of the number of close galaxy pairs owing to the finite size of fibres (55 arcsec on the sky). This 'fibre separation effect' partly eliminates the small-scale clustering of galaxies and artificially reduces the measured richness of highly dense clumps.

3.2 The influence of selection effects on our analyses

As noted above, the construction of the LCRS involves some extraordinary selection effects beyond those associated with conventional magnitude-limited surveys. These added complexities make it especially important to estimate the stability and reliability of our results. Here we discuss the strategy and criteria for such estimates that have been employed in our analyses.

In general, the impact of moderate selection effects on the richer structure elements is not so important because these structures are formed by many galaxies with a variety of luminosities, and thus the main effect on these structures is an artificial decrease in their richnesses. On the other hand, variations in the field-to-field sampling can produce two competing effects in the population of observed low-density structures: firstly, they can eliminate poorer structures completely, and, secondly, they can break apart inhomogeneous richer structures, creating additional sets of artificially poor structures.

Both the NCLL and MST techniques, as well as the percolation approach, deal with the positions of individual galaxies, and therefore can be heavily influenced by variations in sampling. For example, a few additional points suitably placed between larger clumps will link them together and change the characteristics of a small number of richer clusters. The opposite effect can occur if the removal of a few critical points destroys a bridge between two rich clusters. On the other hand, the same number of points added (or removed) within the low-density regions will only slightly change the distribution of the numerous poorer clusters, and the influence on the statistical characteristics of the sample will be negligible.

Both the MST and clustering analysis characterize the *given*

sample of objects, and careful preparation of the sample *before* constructing the MST is required. Hence, to some extent, the results from our analyses are sample dependent. None the less, the degree of sample dependence can be estimated and even mitigated.

Our practice has shown that one of the best ways of estimating and correcting for the effect of sample dependence in our methods is to analyse relatively homogeneous subsamples. If necessary, an independent analysis can be repeated for other subsamples. Furthermore, some properties of the clusters we obtain – for example, their richness – can be corrected for selection effects. Even so, to correct other cluster parameters such as their sizes and possible interconnectedness requires special analysis.

The most robust means of reducing the influence of the main selection effects would be to make use of volume-limited samples. Unfortunately, owing to the LCRS's use of both a bright and faint magnitude limit, it is essentially impossible to extract a homogeneous volume-limited sample of sufficient depth and galaxy number to perform the analyses in this paper.

None the less, we carry a few weapons in our statistical armoury to combat the worst atrocities committed by selection effects. First, we confine our analyses to redshift intervals where – owing to the LCRS's use of both a *bright* and *faint* apparent magnitude limit – the radial selection function is relatively flat (Fig. 1; see also Lin et al. 1996, fig. 7). This reduces the redshift dependence of our results. The influence of this selection changes the cluster richness by about 20 per cent.

Second in our arsenal is the use of suitably normalized dimensionless variables based upon the mean *observed* number density of individual slices and/or samples. This permits the effective removal of the grossest aspect of the variable selection criteria between samples – that of the *mean* selection over an entire slice/sample. Thus, we can make use of our third weapon.
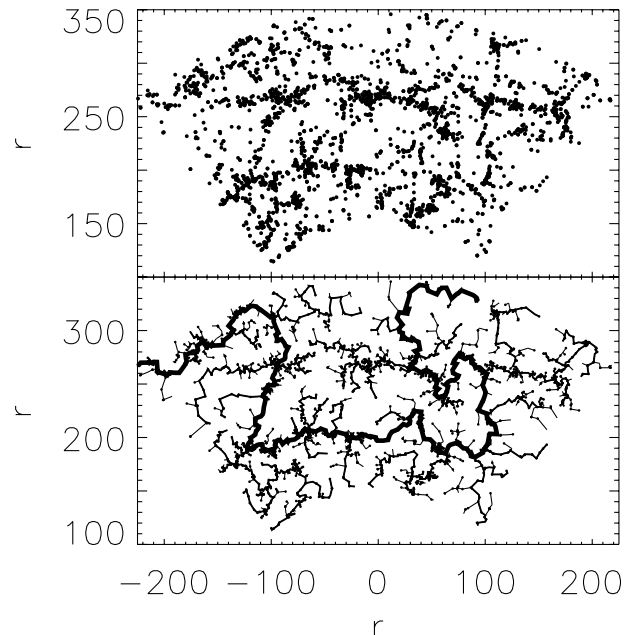

Figure 1. Top, the distribution of galaxies in the LCRS-3 slice in the distance interval $150 \leqslant D \leqslant 350\,h^{-1}\,\mathrm{Mpc}$. Note the relative lack of apparent radial selection effects owing to the moderate flatness of the LCRS selection function over this interval. Bottom, the minimal spanning tree for the above galaxy distribution. The trunk and longer branches of MST are plotted by the thicker lines.

Our third weapon is the actual inter-comparison of results for different slices. Since the LCRS slices range in their level of 50-/112-fibre-field intermixture from that of slice LCRS-3 (all 112-fibre fields) and slice LCRS-2 (nearly all 50-fibre fields) to slices LCRS-1, -4, -5 and -6 (almost a checkerboard pattern of 50- and 112-fibre fields), the inter-comparison of results from the different slices can tell us how robust our results are against field-to-field sampling variations. Furthermore, significant differences among the results for the different slices can act as a warning, alerting us to the fact that we have trespassed into an interval of linking lengths or density thresholds where our techniques break down.

Finally, we can test the effects of the radial selection function on by making a priori corrections to the cluster-finding linking lengths to take into account the selection function. To do this, we create modified LCRS galaxy catalogues, in which we adjust the radial distance to the galaxies. By artificially moving the more distant galaxies in an appropriate manner, we create an artificially volume-limited sample in which a constant linking length may be used for the full sample of galaxies. This is essentially equivalent to using the unmodified LCRS galaxy catalogues and varying the linking length according to the selection function at a given redshift as is accomplished in more conventional 'friends-of-friends' group-finding algorithms (e.g. Huchra & Geller 1982). Specifically, we choose an 'artificial', or modified, radial distance, r_a, for each galaxy using the following equation:

$$r_a^3 = 2R_{sel}^3 \int_0^{x_s} dx\, x\, e^{-x} = 2R_{sel}^3 [1 - (1 + x_s)\, e^{-x_s}], \quad (3.1)$$

$$x_s = (r/R_{sel} - x_0)^{3/2}, \quad R_{sel} \approx 150\, h^{-1} \text{Mpc}, \quad x_0 \approx 0.44,$$

where r is the galaxy's real radial distance, R_{sel} is the typical scale of the radial selection function (Baugh & Efstathiou 1993), and x_0 describes the deficit of galaxies at $r \leqslant 70\, h^{-1}$ Mpc in the LCRS. In such modified catalogues the observed density of galaxies is independent of distance and the random distance variations do not exceed 10 per cent. In these catalogues we can extract clusters at any distance with (approximately) the same efficiency. Of course, this procedure cannot restore lost information, but it does allow us to test the influence of radial selection effects on our measurements of structure properties.

Survey geometry, on the other hand, proves to be a more serious problem. The angular width of a slice is only $1°.5$, corresponding to a linear dimension of ~ 6–$7\, h^{-1}$ Mpc at the typical sample depths used. The relative thinness of the slices is important as it destroys evidence of both the filamentary network and the curved wall-like structure elements. The total effect cannot be estimated a priori, and even comparison with simulations does not help substantially. Such a comparison has shown that this factor certainly distorts the properties of even rich walls, but the estimated level of distortion depends upon the simulation used. Moreover, simulations indicate that the LCRS slices are not large enough to encompass a sufficiently representative sample of structure elements to depress slice-to-slice variations in their measured properties.

The selection effects inherent to the LCRS, its survey geometry and its limited number of galaxies certainly place obstacles in the path of our methods of analysis, distorting the resulting measured properties of the galaxy distribution on very large scales. Thus, the quantitative characteristics obtained below can be considered as typical only for the LCRS. These measurements can be partly corrected by the comparison with available simulations, but this problem cannot be completely resolved until yet larger redshift surveys become available. Bearing these comments in mind, we

will concentrate below more on the investigation of the richer structure elements: for these, the selection effects are less important, although some of our more qualitative results can still show a weak sensitivity to moderate variations in selection criteria.

3.3 Characteristics of the galaxy distribution derived from the PDF MST and NCLL techniques

As a first step, the analysis has been performed for each of the six slices over two different ranges in distance – $150 \leqslant D \leqslant 350\, h^{-1}$ Mpc (LCRS-350) and $150 \leqslant D \leqslant 450\, h^{-1}$ Mpc (LCRS-450). This
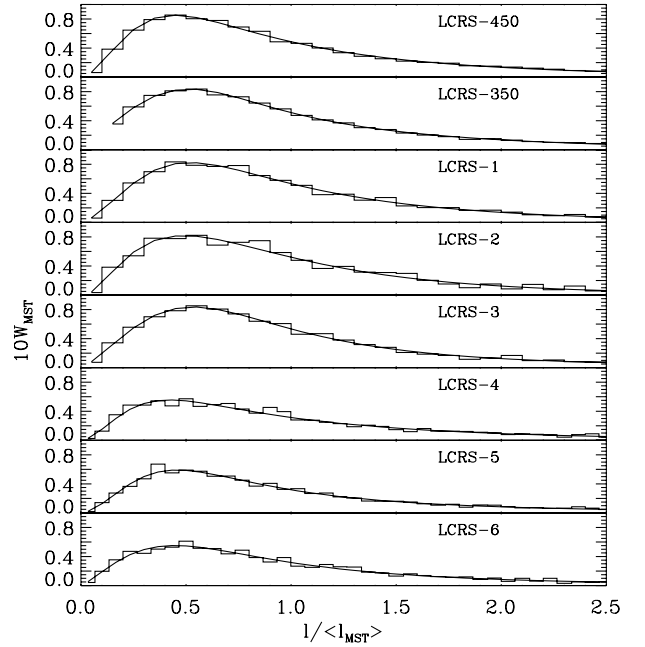

Figure 2. The PDF MSTs averaged over six slices for two full samples (LCRS-450 and LCRS-350) and for the six separate slices of LCRS-350. The best fits (2.4) are plotted by the solid line.
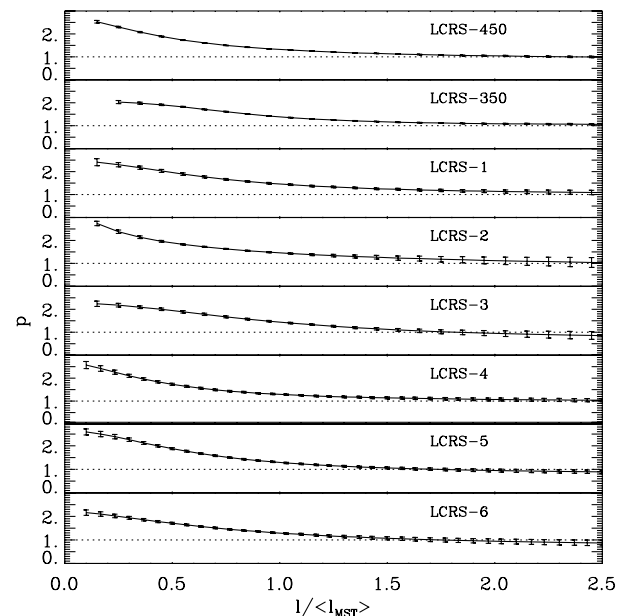

Figure 3. Functions p_{MST} (2.2) for the PDF MSTs plotted in the previous figures.

allows us both to obtain the general characteristics of the structure and to estimate the influence of observational selection effects on the structure properties. The first sample – LCRS-350 – includes about 80 per cent of the galaxies from the second, but at only 45 per cent of the volume. Thus, the mean number density of observed galaxies for the second sample is about twice that of the first. As an additional test of the robustness of our methods against selection effects, a most distant part of the survey, with $350 \leqslant D \leqslant 450\,h^{-1}$ Mpc, was analysed separately.

The main results obtained with the NCLL and MST techniques are plotted in Figs 2–4 and listed in Table 1. In Fig. 2, we plot the PDF MSTs together with six-parameter fits (2.4) for each of the six slices of the LCRS-350 sample. Furthermore, in the top two panels of this figure, we plot the joint PDF MSTs for the LCRS-350 and for the LCRS-450 samples; these joint PDF MSTs are generated by averaging the individual PDF MSTs from each of the
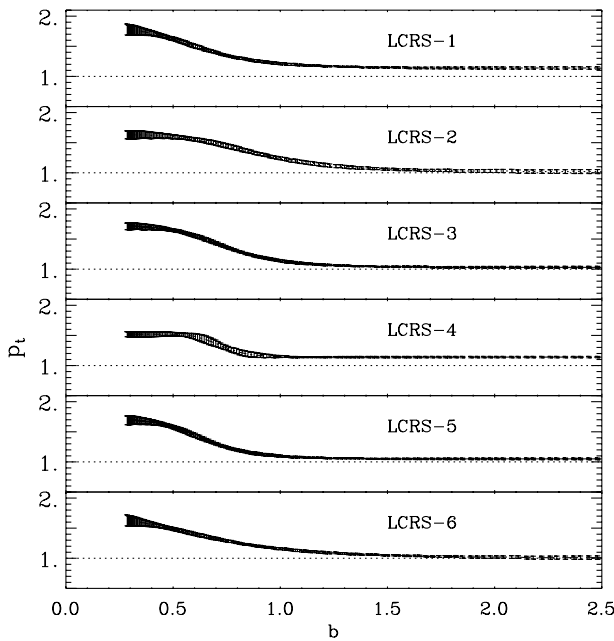
six slices. Note that the use of the dimensionless relative variable $l/\langle l_{\mathrm{MST}} \rangle$ – rather than the edge length l itself – eliminates the influence of slice-to-slice variations in the mean observed galaxy density, emphasizes the joint properties of the PDF MSTs and permits the construction of the joint PDF MSTs for the two full samples. Variations in the power indices p_{MST} for the same samples are plotted in Fig. 3. Owing to the rather illustrative character of this figure the plotted error bars were estimated under the assumption of a normal distribution of errors using the covariance matrix of the fitted parameters.

These figures demonstrate that the PDF MSTs are similar for all the cases under consideration. The interval $l \lesssim 0.5\langle l_{\mathrm{MST}} \rangle$ includes ~20 per cent of the edges found in the various PDF MSTs and is characteristic of the inner structure of high-density clusters. The properties of this region of the PDF MST shows slight variations among the slices. None the less, in all cases a maximum is reached for $l \sim 0.5\langle l_{\mathrm{MST}} \rangle$, and, for the significant fraction of larger edges (the ~40 per cent of edges that have $l \geqslant \langle l_{\mathrm{MST}} \rangle$), a joint exponential distribution with $p_{\mathrm{MST}} \approx 1$ is found. This demonstrates that in all the slices the spatial distributions of the larger edge lengths, $l \geqslant \langle l_{\mathrm{MST}} \rangle$, are similar to a 1D Poisson distribution. It can be interpreted as evidence in favour of a 1D filamentary distribution of galaxy and clusters for larger l. This inference relates mainly to the underdense regions because for such edge lengths the number of massive clusters is relatively small.

The asymptotic values of p_{MST} for both the full samples and for the individual slices of LCRS-350 and LCRS-450 are listed in Table 1 together with the dimensional and dimensionless mean edge lengths, $\langle l_{\mathrm{MST}} \rangle$ and $\langle b_{\mathrm{MST}} \rangle$, defined by (2.3). Variations of the dimensionless parameters from slice to slice do not exceed a few per cent. The errors listed for p_{MST} were found using a one-parameter fit (2.3) over the interval $l \geqslant \langle l_{\mathrm{MST}} \rangle$ for the values of W_0 and α_{MST} taken from the best three-parameter fit (2.3). These estimates were repeated for various bin sizes and p_{MST} was found to be only weakly dependent on such variations.

The very smooth exponential behaviour of the PDF MSTs for $l \geqslant 0.5\langle l_{\mathrm{MST}} \rangle$ does not permit an interpretation of conspicuous percolation (see, however, Shandarin & Yess 1998). Clearly, no evidence can be found for an abrupt onset of percolation up to linking lengths of $b \sim 2$–2.5, at which point the single largest cluster in a slice incorporates ~ 20–30 per cent of all galaxies. This result confirms that galaxies tend to be concentrated within a

Figure 4. Functions p_{cl} (2.2) versus dimensionless linking length b for the six slices of the LCRS-350.

Table 1. Fit parameters for the NCLL and PDF MST analyses for the six individual slices and for the two full samples of the LCRS-450 and LCRS-350.

	N_{gal}	$10^3 \langle n_{\mathrm{gal}}^{\mathrm{obs}} \rangle$ $h^3\,\mathrm{Mpc}^{-3}$	$\langle l_{\mathrm{MST}} \rangle$ $h^{-1}\,\mathrm{Mpc}$	$\langle b_{\mathrm{MST}} \rangle$	p_{MST}	p_{cl}
			$150 \leqslant D \leqslant 450\,h^{-1}\,\mathrm{Mpc}$			
LCRS-450	21 352	3.35	3.0	0.72	0.99 ± 0.05	1.0 ± 0.05
LCRS-1	3716	3.52	3.0	0.73	1.10 ± 0.04	1.0 ± 0.03
LCRS-2	2176	2.19	3.9	0.82	1.02 ± 0.07	1.0 ± 0.02
LCRS-3	4394	4.34	2.8	0.77	1.06 ± 0.04	1.1 ± 0.02
LCRS-4	3524	3.07	3.1	0.73	1.05 ± 0.05	1.1 ± 0.02
LCRS-5	4012	3.68	2.8	0.70	0.93 ± 0.04	1.0 ± 0.02
LCRS-6	3530	3.30	2.9	0.70	1.09 ± 0.05	1.0 ± 0.03
			$150 \leqslant D \leqslant 350\,h^{-1}\,\mathrm{Mpc}$			
LCRS-350	16 756	5.65	2.6	0.75	1.05 ± 0.04	1.06 ± 0.06
LCRS-1	3040	6.19	2.6	0.77	1.08 ± 0.09	1.1 ± 0.02
LCRS-2	1778	3.84	3.4	0.86	1.01 ± 0.21	1.0 ± 0.04
LCRS-3	3395	7.21	2.4	0.77	0.88 ± 0.12	1.0 ± 0.02
LCRS-4	2783	5.22	2.6	0.73	1.03 ± 0.07	1.1 ± 0.01
LCRS-5	3171	6.22	2.4	0.71	0.91 ± 0.07	1.1 ± 0.01
LCRS-6	2589	5.26	2.5	0.70	0.89 ± 0.11	1.0 ± 0.03

small number of *separate* massive clusters. This effect is enhanced by the LCRS construction as a set of relatively thin slices, which is demonstrated by a similar analysis performed on the DURS, on the DMRT, and on the available mock catalogues (CHWF). In contrast to the LCRS, for all of these other cases percolation takes place at $b = b_{perc} \sim 1.2$.

Results obtained with the NCLL method are plotted in Fig. 4 and listed in Table 1. The slice-to-slice variations of the power index $p_{cl}(b)$ at $b \lesssim 1$ is a quantitative measure of objective differences in the galaxy distributions within denser clusters and in their successive integrations into the joint structure network. Of course, these inferences relate to the number of clusters rather than to the fraction of galaxies. Even so, the power index $p_{cl} \approx 1$ appears for $b \gtrsim 1$, when only ~ 65 per cent of galaxies are incorporated in clusters with a richness $N_{mem} \gtrsim 5$ and only ~ 5–7 per cent of galaxies are accumulated by the richest cluster. Therefore, these results are reasonably representative of the large-scale galaxy distribution in the LCRS and actually reveal a 1D character of the joint network which is composed of a set of clusters with various richness bridged by filamentary-like elements. The power indices, p_{cl}, obtained for $b \gtrsim 1$ by averaging over six slices, are also listed in Table 1. The error bars for p_{cl} plotted in Fig. 4 and listed in Table 1 were found in the same manner as before. These errors are less than those found with the MST technique because the cluster number is the cumulative PDF with respect to the PDF of MST edges.

Of course, such a geometrical interpretation is not obligatory. The results imply only that the number of clusters varies with linking length identically to the case of a Poisson point distribution for the corresponding dimension. Actually the index p_{cl} characterizes only the edge distribution in the MST and is identical to the power indices p_{MST} in Table 1 (they differ only by the fitting procedure, which allows us to test for the precision attained).

4 STRUCTURE ELEMENT PARAMETERS

The analysis performed above does not reveal significant differences between the LCRS-350 and LCRS-450 samples for the dimensionless parameters $\langle b_{MST} \rangle$, p_{MST} and p_{cl}. None the less, to diminish the influence of radial selection effects and thereby to obtain a better measure of the relative abundances of clusters of different richnesses, we will only consider the LCRS-350 sample in what follows. The LCRS-350 sample includes most of the richer clusters from the larger LCRS-450 sample. The relative deficit of these clusters at larger distances is most likely to be caused by random variations in the spatial galaxy distribution, but it can be reinforced by the radial selection effects inherent in a flux-limited survey.

Here, we are interested in the properties of structure elements formed by the set of all clusters defined by a given linking length b_{thr}. Clearly, the properties of these structure elements will depend on the particular threshold linking length chosen for cluster identification. The analysis performed in Section 3 can be used to choose a suitable range of b_{thr} for the identification of structure elements. The PDF MST is significantly different for $l/\langle l_{MST} \rangle \lesssim 0.5$, $b \lesssim 0.4$ and for $l/\langle l_{MST} \rangle \gtrsim 1$, $b \gtrsim 0.8$, at which point the shape of PDF MST becomes universal. This behaviour of the PDF MST points out a natural threshold value to use for the conventional identification of structure elements in the LCRS-350: $b_{thr} \gtrsim 0.8$.

Table 2. Mean parameters of clusters with $N_{thr} \geqslant 5$ in the LCRS-350.

	N_{cl}	$\langle N_{mem} \rangle$	$\langle V_{cl} \rangle$ $h^{-3}\,\mathrm{Mpc}^3$	f_s	$f(\geqslant 5)$
		$b_{thr} = 1$			
LCRS-1	137	15.3	2500	0.14	0.69
LCRS-2	99	11.1	2900	0.16	0.62
LCRS-3	126	18.3	2500	0.14	0.68
LCRS-4	134	14.6	2800	0.13	0.70
LCRS-5	140	16.8	2700	0.11	0.73
LCRS-6	127	14.7	2800	0.13	0.72
		$b_{thr} = 1.25$			
LCRS-1	133	18.5	3000	0.08	0.81
LCRS-2	100	13.7	3560	0.09	0.77
LCRS-3	107	25.9	3590	0.08	0.79
LCRS-4	130	17.4	3330	0.08	0.81
LCRS-5	122	21.2	3400	0.08	0.81
LCRS-6	109	20.1	3820	0.08	0.85

As discussed above, for the LCRS the onset of percolation does not restrict our choice of b_{thr}, and the properties of the structure elements vary gradually for larger $b_{thr} \gtrsim 0.8$. In contrast, for smaller b_{thr}, the fractions of poorer clusters and single galaxies increase rapidly and the linking lengths $b \lesssim 1$ can be used to investigate the subpopulation of high-density cores and the intrinsic structure of larger clusters.

Further analysis confirms that for the LCRS the interval $b_{thr} \sim$ 1–1.3 is best suited for such identification; thus, we will consider this region in more detail and will use mainly two dimensionless threshold linking lengths, namely $b_{thr} = 1$, and $b_{thr} = 1.25$. In particular, we consider just these two values of b_{thr} in Table 2, in which we tabulate the following properties of the resulting cluster samples:

(i) the number of clusters within a slice, N_{cl};
(ii) the mean cluster richness, $\langle N_{mem} \rangle$;
(iii) the mean cluster volume,

$$\langle V_{cl} \rangle = \langle N_{mem} \rangle / \langle n_{gal} \rangle, \tag{4.1}$$

where $\langle n_{gal} \rangle$ is taken from Table 1;
(iv) the fraction of single galaxies, f_s; and
(v) the fraction of galaxies incorporated into the structure elements with $N_{mem} \geqslant 5$, $f(\geqslant 5)$.

(For clusters with $N_{mem} \lesssim 5$ the parameters from our methods of statistical description become unreliable.)

The parameters listed in Table 2 show, for both values of b_{thr}, that the fraction of single galaxies is less than 10–15 per cent and that the clusters with $N_{mem} \geqslant 5$ contain ~ 70–80 per cent of all galaxies. In each slice, ~ 40–50 per cent of galaxies are concentrated within the 20–30 richest clusters (Section 5). Slice-to-slice variations in $\langle N_{mem} \rangle$ are proportional to slice-to-slice variations in the mean observed galaxy density, $\langle n_{gal} \rangle$ (Table 1). Slice-to-slice variations in $\langle V_{cl} \rangle$, however, are proportionally less:

$$\langle V_{cl} \rangle = (2.7 \pm 0.15) \times 10^3 \, h^{-3}\,\mathrm{Mpc}^3, \quad b_{thr} = 1, \tag{4.2}$$

$$\langle V_{cl} \rangle = (3.45 \pm 0.25) \times 10^3 \, h^{-3}\,\mathrm{Mpc}^3, \quad b_{thr} = 1.25. \tag{4.3}$$

These estimates for $\langle V_{cl} \rangle \propto b_{thr}$ as well as the estimates for f_s and $f(> 5)$ confirm that in all slices and for both threshold linking lengths the structure properties are quite similar. They demonstrate that the influence of field-to-field sampling variations, of the 'fibre separation effect', and of random selection of galaxies is

relatively small. Larger slice-to-slice variations, however, are evident in the characteristics of the richest walls (Section 5.2).

To test further the influence of usual selection effects on the measured structure properties and to estimate the robustness of measured values for the structure parameters, the analysis was repeated using the modified catalogues described by (3.1) for depths of $150 \leqslant D \leqslant 450\,h^{-1}$ Mpc. This approach cannot make up lost information and the reliability of the results obtained from such catalogues is questionable. None the less, it allows us to discriminate between the impact on our results from the sample properties and from radial selection effects. The analysis shows that the fractions of matter, f_s and $f(>5)$, remain the same as those listed in Table 2, whereas the number of clusters, N_{cl}, increases by a factor of ~ 1.3–1.5 (this is caused by the increase in the sample volume). The mean richness of the clusters drops by ~ 10–15 per cent for $b_{thr} = 1$ but remains almost the same for $b_{thr} = 1.25$. The mean volume of clusters in the 'artificial' space, $\langle V_a \rangle$, is found to be

$$\langle V_a \rangle = (2.7 \pm 0.36) \times 10^2\,h^{-3}\,\text{Mpc}^3, \quad b_{thr} = 1, \tag{4.4}$$

$$\langle V_a \rangle = (3.64 \pm 0.35) \times 10^2\,h^{-3}\,\text{Mpc}^3, \quad b_{thr} = 1.25 \tag{4.5}$$

and slice-to-slice variations are relatively small (as was the case with the non-modified LCRS galaxy catalogues).

The results obtained for these modified catalogues shows that the more general characteristics of clustering process listed in Table 2 are representative and robust. The growth in the dispersions in V_a relative to (4.2) and (4.3) shows that the corrections for radial selection effects do not significantly improve upon our original, uncorrected results.

Stronger variations (~ 15–20 per cent), however, arise for the properties of the richer clusters as discussed below. These variations demonstrate again that even a sample composed by ~ 2000–3000 of galaxies located in a volume $\sim 10^6\,h^{-3}\,\text{Mpc}^3$ cannot yet provide precisions better than about 20 per cent for measured characteristics of the large-scale galaxy distribution. These comments refer primarily to the mass function discussed in the next subsection, but they also suggest that the cosmic variance of structure properties can be possibly seen as a modulation of structure characteristics – and first of all as a modulation in the characteristics of the rarer and richer wall-like elements – with typical scales of $\sim 100\,h^{-1}$ Mpc.

4.1 The mass function of the structure elements

An important characteristic of the structure is the richness distribution (mass function) of clusters

$$W_m(b, N_{mem}) = \frac{N_{mem}}{N_{gal}} N_{cl}(\mu_m), \quad \mu_m = \frac{N_{mem}}{\langle N_{mem} \rangle}, \tag{4.6}$$

where N_{cl} is the number of clusters with N_{mem} galaxies, N_{gal} is the number of galaxies in the sample and $\langle N_{mem} \rangle$ is the mean cluster richness. To supress the influence of radial selection effects the mass functions were measured for clusters extracted from the LCRS-450 catalogue in which the radial positions were modified according to the prescription of equation (3.1). Using both the modified catalogue and the dimensionless parametrization of the mass function in equation (4.6), we can partly depress the influence of radial selection effects and of variations in the slice parameters (~ 10 per cent); thereby, we may reveal typical properties of the samples under consideration. (Unfortunately, though, we cannot suppress the influence owing to the thinness of the LCRS slices,
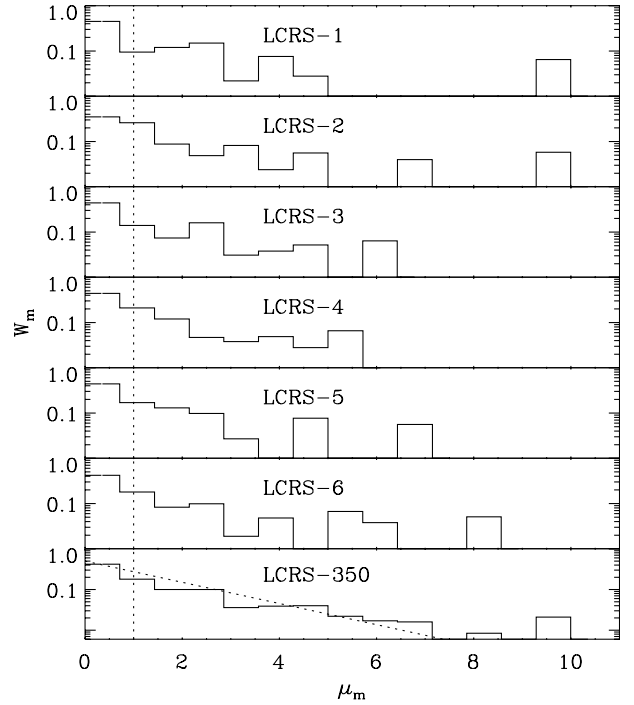

Figure 5. The mass function W_m versus the normalized richness of clusters, μ_m, for the linking length $b = 1.25$ for each of the six slices and for the full sample (bottom panel).

which destroys structure elements and increases the fraction of poorer clusters.)

The mass function was measured for each of the slices using a few different values of $b_{thr} \geqslant 1$. The mass function for $b = 1.25$ is plotted in Fig. 5 for each of the six slices and for the full modified LCRS-450 sample. The mass function $W_m(\mu_m)$ for the full sample was obtained by averaging of individual mass functions for the same μ_m. The resulting distribution can be fitted to the simple expression (Fig. 5)

$$W_m(\mu_m) \propto \mu_m^{-1.15}. \tag{4.7}$$

Note that the general shape of the mass function, $W_m(\mu_m)$, is similar for all slices. Furthermore, it does not change significantly in the range $b_{thr} \sim 1$–1.3, even though the mean richnesses N_{mem}^m and the local threshold densities bounding the clusters vary by factors of ~ 2. This fact confirms that, although the radial selection effects and the variation of the slice parameters do strongly affect the mean characteristics of the mass functions (e.g. $\langle N_{mem} \rangle$), they do not drastically change the shape of the dimensionless mass function, $W_m(\mu_m)$ – at least for $\mu_m \leqslant 4$–5, where the sample of clusters is sufficiently representative. The high concentration of galaxies within poor clusters having $\mu_m \leqslant 1$–1.5 is a natural consequence of the definition of μ_m.

The variations at larger $\mu_m = N_{mem}/\langle N_{mem} \rangle$ are caused by the small statistics for richer clusters and are enhanced by the peculiarities of the LCRS. The existence of such clusters with $\mu_m \sim 5$–10 is typical for all slices in the interval $b_{thr} \approx 1$–1.3. The analysis of other observed and simulated catalogues (DURS, DMRT, CHWF) confirms that for larger μ_m this distribution is strongly sample dependent.

The mass function is more sensitive to the field-to-field variations and to the thinness of the LCRS slices, which destroy

Table 3. Proper sizes and morphology of structure elements.

b_{thr}	N_{thr}	N_{cl}	$\langle N_{mem}\rangle$	$\langle\lambda\rangle$	σ_λ	p_λ	$\langle\omega\rangle$	σ_ω	p_ω	$\langle\theta\rangle$	σ_θ	p_θ	$\langle D_{prw}\rangle$	σ_{prw}	$\langle\epsilon\rangle$	σ_ϵ
1.0	10	361	25.1	17.4	4.9	0.47	8.4	2.1	0.47	3.7	1.3	0.41	19.6	1.5	0.63	0.11
1.0	20	162	39.6	21.5	6.0	0.50	10.4	2.5	0.47	4.5	1.3	0.17	22.4	1.7	0.57	0.09
1.25	10	361	31.5	24.1	7.0	0.50	11.4	3.1	0.51	4.4	1.5	0.31	20.0	2.1	0.61	0.09
1.25	20	179	50.5	30.4	8.7	0.53	14.5	3.9	0.51	5.2	1.5	0.11	22.8	2.4	0.54	0.08

Values $\langle\lambda\rangle$, $\langle\omega\rangle$, $\langle\theta\rangle$ and $\langle D_{prw}\rangle$ and their dispersions are given in h^{-1} Mpc.

the observed structure elements. This means that the numerical estimates given above can be distorted. Even so, the most interesting result of this analysis – the smooth shape of the mass function over a wide interval of μ_m – is confirmed in the analysis of simulations and indicates that the large-scale matter distribution is probably formed due to a joint continual process such as the successive merging of fewer structure elements.

4.2 The proper sizes of the structure elements

The proper sizes of structure elements – the length, L, width, w, and thickness, t – can be found with the inertia tensor method. These parameters also depend on the linking length, b_{thr}, and on the threshold richness, N_{thr}, used in the extraction of the clusters. In spite of this, the resulting values for these parameters are found to be sufficiently stable for use in the statistical description of the observed large-scale galaxy distribution.

A caveat should, however, be mentioned: an additional complication lies in the use of redshift survey data to derive these proper sizes. Redshift survey galaxy distances are convolved with peculiar and streaming motions. Therefore, our measurements of L, w and t from the LCRS will tend to be distorted from their 'true' values. None the less, we expect these distortions to be rather small relative to the values themselves, especially for the larger dimensions, L and w (see, for example, the discussion in DMRT).

For the LCRS-350 sample, the proper sizes were found for two values of b_{thr} and for two values of N_{thr}. For clusters with $N_{thr} \geqslant 10$ in the interval $1 \leqslant b_{thr} \leqslant 1.25$, the sizes of structure elements can be described by the following:

$$L = \lambda\mu_m^{p_\lambda}, \quad w = \omega\mu_m^{p_\omega}, \quad t = \theta\mu_m^{p_\theta}. \tag{4.8}$$

$$\mu_m = N_{mem}/\langle N_{mem}\rangle, \quad p_\lambda = p_\omega = 0.5 \pm 0.03.$$

The mass dependence of the two larger proper sizes, $p_\lambda \approx p_\omega \approx 0.5$ (Table 3) exceeds that expected for regular compact clusters ($p_\lambda \approx p_\omega \approx p_\theta \approx 0.33$) and that found in simulations (DMRT). This result agrees well with estimates obtained for the DURS (Doroshkevich et al. 2000) and demonstrates the strong correlation between cluster sizes and richnesses. The weaker mass dependence of the thickness, t, is caused by the finite thickness of the LCRS slices, which restricts the thickness of rich clusters.

The mean values and dispersions for the functions λ, ω and θ are listed in Table 3. Averaging has been performed over all the clusters and over all the slices. Each cluster was weighted by the *observed* number of cluster members N_{mem}, which allows us to obtain the parameters typical for the majority of galaxies. The distribution functions of λ, ω and θ plotted in Fig. 6 for $b_{thr} = 1.25$ and $N_{thr} = 10$ have been fit to the Gaussian distributions with the mean values and dispersions listed in Table 3. For each slice the same parameters are listed in Tables 4 and 5 for the richest clusters and the richest walls alone.
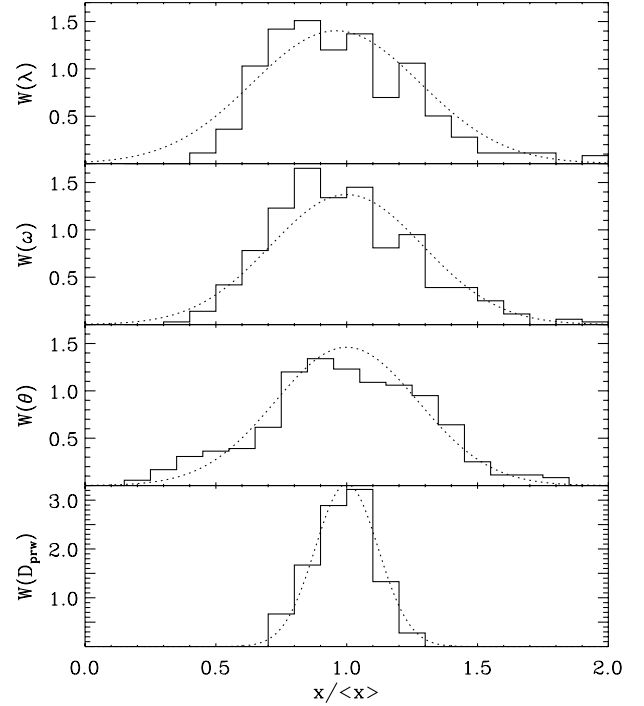

Figure 6. For $b_{thr} = 1.25$ and $N_{thr} = 10$ distribution functions $W(\lambda)$, $W(\omega)$, $W(\theta)$ and $W(D_{prw})$, are plotted versus their argument normalized over the mean value. The Gaussian functions with parameters listed in Table 3 are plotted by dotted lines.

The parameters listed in Table 3 are reasonably stable and the variations in mean values and dispersions as a function of N_{thr} and b_{thr} characterize the procedure used in identifying structure elements. In the range $0.8 \leqslant b_{thr} \leqslant 1.3$ this dependence can be roughly fitted to expressions

$$\langle\lambda\rangle \propto \langle\omega\rangle \propto b_{thr}^{3/2}, \quad \sigma_\lambda/\langle\lambda\rangle \approx \sigma_\omega/\langle\omega\rangle \approx 0.3,$$

$$\langle\theta\rangle \propto b_{thr}, \quad \langle N_{mem}\rangle \propto b_{thr}.$$

4.3 The proper sizes of protowalls

The measured proper sizes of the walls allow us to estimate both their mean overdensity with respect to the mean density of galaxies, δ, and the proper sizes of the protowalls, R_{prw}, the compression of which produces the observed structure elements. The mean overdensity is defined as

$$\delta = \frac{6N_{mem}}{\pi Lwt\langle n_{gal}^{obs}\rangle} \tag{4.9}$$

and for the LCRS the typical overdensity of structure elements for

Table 4. Mean parameters of the richer clusters for the LCRS-350.

	N_{thr}	N_{cl}	$\langle N_{mem}\rangle$	$\langle\lambda\rangle$	σ_λ	p_λ	$\langle\omega\rangle$	σ_ω	p_ω	$\langle\theta\rangle$	σ_θ	p_θ	$\langle D_{prw}\rangle$	σ_{prw}	$\langle\epsilon\rangle$	σ_ϵ
						$b_{thr}=1$										
LCRS-1	14	40	33.3	19.7	5.4	0.4	9.7	1.8	0.5	4.8	1.4	0.3	20.8	1.2	0.60	0.1
LCRS-2	10	39	18.1	17.0	4.1	0.5	8.6	1.8	0.4	4.1	1.2	0.4	20.3	0.6	0.71	0.1
LCRS-3	20	34	45.5	20.8	5.0	0.6	11.0	2.2	0.6	5.1	1.3	0.3	22.0	1.0	0.52	0.1
LCRS-4	16	40	30.0	19.2	5.8	0.4	9.0	2.8	0.5	3.8	1.1	0.2	21.5	1.0	0.62	0.1
LCRS-5	20	37	38.1	20.4	6.2	0.7	9.4	2.3	0.6	3.7	1.1	0.2	21.6	1.4	0.57	0.1
LCRS-6	15	37	31.6	20.9	5.0	0.6	9.0	2.5	0.5	4.0	1.0	0.2	21.6	1.2	0.59	0.1
LCRS-350	–		32.1	19.9	5.6		9.5	2.3		4.3	1.3		21.4	1.6	0.59	0.1
						$b_{thr}=1.25$										
LCRS-1	23	28	46.4	23.5	6.1	0.4	12.8	3.0	0.4	5.9	1.5	0.1	23.3	1.4	0.55	0.1
LCRS-2	16	18	33.2	27.3	7.9	0.7	12.2	2.7	0.1	5.8	1.4	0.1	23.8	2.0	0.62	0.1
LCRS-3	32	18	83.9	34.5	6.4	0.8	17.6	3.0	0.5	6.5	1.1	0.0	24.8	1.8	0.45	0.1
LCRS-4	20	30	39.3	27.3	1.4	0.3	11.9	3.4	0.4	4.4	1.3	0.1	22.4	2.6	0.59	0.1
LCRS-5	32	25	55.3	28.6	7.7	0.6	13.7	3.9	0.6	4.3	1.1	0.1	23.5	1.9	0.51	0.1
LCRS-6	35	13	67.4	35.4	6.7	0.8	16.3	5.0	0.7	5.0	1.0	0.0	25.5	1.6	0.50	0.1
LCRS-350	–		55.2	35.2	10.9		16.9	4.2		6.3	1.4		24.0	2.9	0.52	0.1

Mean values and dispersions of clusters sizes are given in h^{-1} Mpc.

Table 5. Parameters of the richest walls.

	N_{mem}^{max}	L_{max}	w_{max}	t_{max}	R_{prw}^{max}
			$b_{thr}=1$		
LCRS-1	169	53.2	19.5	4.7	23.7
LCRS-2	94	38.5	14.0	4.5	24.5
LCRS-3	151	41.9	16.6	6.7	21.5
LCRS-4	91	21.3	14.2	3.6	22.5
LCRS-5	124	38.9	18.9	3.6	24.5
LCRS-6	112	44.8	15.0	4.9	23.2
			$b_{thr}=1.25$		
LCRS-1	170	53.2	19.7	4.8	23.7
LCRS-2	94	38.5	14.0	4.5	24.5
LCRS-3	213	74.0	28.1	6.3	21.5
LCRS-4	91	21.3	14.2	3.6	22.5
LCRS-5	215	61.9	22.6	4.2	24.4
LCRS-6	179	72.8	26.6	5.4	23.4

Values L_{max}, w_{max}, t_{max} and R_{prw}^{max} are given in h^{-1} Mpc.

$b_{thr} \sim 1$–1.3 is $\delta \approx 5$–10. This means that these structure elements were formed by non-linear matter compression.

For the larger walls the compression along the largest axes is small and we can characterize the proper sizes of protowalls, R_{prw}, by a characteristic size of prolate spheroid whose 2D (anisotropic) compression results in the formation of the observed wall. This estimate assumes that $R_{prw} \leqslant L$ because otherwise 3D compression must be taken into consideration. To obtain the proper size of the protowall, the 2D conservation law of the number of galaxies may be applied. Here we define the size $R_{prw}(N_{mem})$ of a structure element of given richness N_{mem} as the size of prolate spheroid with the diameter L containing the mean observed density of galaxies in the slice, $\langle n_{gal}^{obs}\rangle$. Thus,

$$R_{prw}^2 = \langle\delta wt\rangle = \langle w_{prw}t_{prw}\rangle = \frac{6N_{mem}}{\pi L\langle n_{gal}^{obs}\rangle}, \quad (4.10)$$

where w_{prw} and t_{prw} are the comoving width and thickness of the protowall for a homogeneous galaxy distribution.

The parameter R_{prw} was found for the same samples described above under the condition that $R_{prw} \leqslant L$. The analysis shows that R_{prw} is well fitted by the expression

$$R_{prw}(N_{mem}) = D_{prw}\mu_m^{p_w}, \quad p_w = 0.25 \pm 0.02, \quad (4.11)$$

which describes R_{prw}'s richness dependence. The distribution of D_{prw} is plotted in Fig. 6 and fits well to a Gaussian distribution having the mass-weighted means and dispersions listed in Table 3. For the richer and richest walls the values for R_{prw} are listed slice-by-slice in Tables 4 and 5.

Values for $\langle D_{prw}\rangle$ do not vary by more than 10 per cent over the range $0.8 \leqslant b_{thr} \leqslant 1.6$ and their slice-to-slice variations are less than for the two larger proper sizes because the variations in N_{mem} and L are usually correlated.

4.4 The morphology of the structure elements

As was described in Sections 2.3 and 2.4 the morphology of the structure elements can be characterized *quantitatively* with the inertia tensor method for the more regular clusters (those which can be approximated by a convex ellipsoid), and by the ratio L_{tr}/L_{sum}, where L_{sum} and L_{tr} are, respectively, the full length of the MST edges and the length of the trunk that is the maximal path of the tree. The inertia tensor method can be applied to most richer clusters and to some fraction of the compact filaments. This method, however, is strongly sensitive to random variations of cluster shape and the resulting estimates $\langle w/L\rangle \approx \langle t/w\rangle \sim 0.5 \pm 0.2$ are weakly dependent on the linking length used for the cluster identification and on cluster richness.

The other measure, L_{tr}/L_{sum}, is more sensitive to the cluster richness: for poorer clusters, $L_{tr}/L_{sum} \approx 1$, but, for richer clusters, $L_{tr}/L_{sum} \leqslant 0.5$ is typical. For the full sample of clusters the richness dependence of this characteristic can be fitted to the power law

$$L_{tr}/L_{sum} = \epsilon\mu_m^{-p_\epsilon}, \quad p_\epsilon = 0.25 \pm 0.01, \quad (4.12)$$

where μ_m was defined by (4.6)

We list in Table 3 the means $\langle\epsilon\rangle$ and the dispersions σ_ϵ for two values of N_{thr} and two values of b_{thr}. The distribution function $W(\epsilon)$ is plotted in Fig. 7. It is well fitted to a Gaussian function with the values of $\langle\epsilon\rangle$ and σ_ϵ listed in Table 3. Over the range $0.8 \leqslant b_{thr} \leqslant 1.6$ the variations of $\langle\epsilon\rangle$ can be fitted approximately by the expression

$$\langle\epsilon\rangle \approx 0.75(1 - 0.16b_{thr}).$$

The relatively high stability and small dispersion of this measure confirm the systematic continuous dependence of

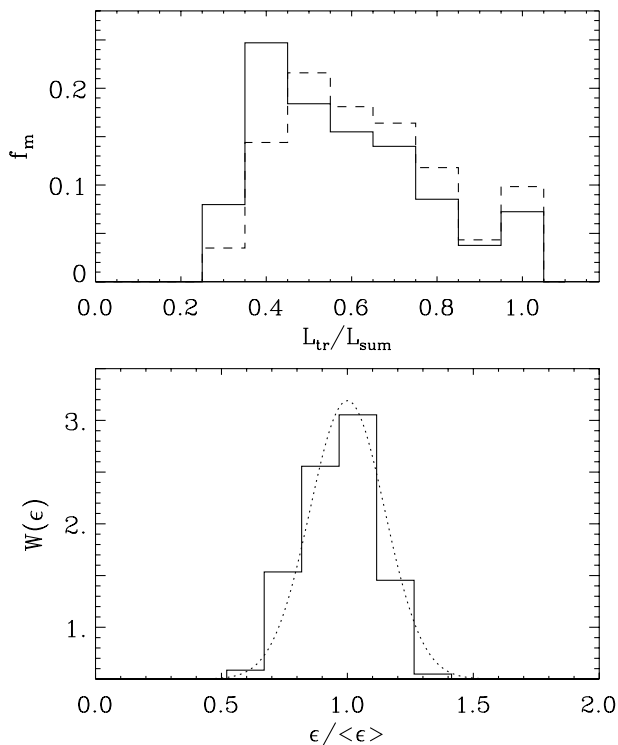**Figure 7.** Top, the mass distribution versus L_{tr}/L_{sum} are plotted for $N_{thr} = 5$ and $b_{thr} = 1.25$ (solid line) and $b_{thr} = 1$. (dashed line). Bottom, the distribution function $W(\epsilon)$ versus $\epsilon/\langle\epsilon\rangle$ for $b_{thr} = 1.25$ and $N_{thr} = 10$. The Gaussian functions with parameters listed in Table 3 are plotted by dotted lines.

morphology on the cluster richness and characterize it statistically. For all the slices the sheet-like or elliptical elements with the ratio $L_{tr}/L_{sum} \leqslant 0.5$ are found to be dominant for the richer clusters, whereas, for poorer clusters, a filamentary-like component with $1 \geqslant L_{tr}/L_{sum} \geqslant 0.7$–$0.8$ prevails.

The fraction of galaxies, f_m, concentrated within clusters with a given L_{tr}/L_{sum} is also plotted in Fig. 7 for two samples of clusters with $N_{thr} = 5$ and $b_{thr} = 1$ (dashed line) and $b_{thr} = 1.25$ (solid line). This figure demonstrates that for such b_{thr} and $N_{thr} \sim 40$–50 per cent and ~ 30 per cent of all galaxies of LCRS-350 are incorporated within clusters with $L_{tr}/L_{sum} \leqslant 0.5$ and $L_{tr}/L_{sum} \geqslant 0.7$, respectively.

5 PROPERTIES OF RICHER STRUCTURE ELEMENTS

In Paper I, we showed through a core-sampling analysis that structure elements fall naturally into two distinct populations, one of which is seen as a set of richer and denser clumps forming sheet-like structures and the other of which is composed of poorer and less dense clusters forming filamentary structures. In that paper, we estimated that these subpopulations incorporate ~ 60 per cent and ~ 40 per cent of galaxies, respectively. The spatial distribution of these two subpopulations, characterized by the mean free path between elements of each, was also found to be very different.

The core-sampling method (Buryak et al. 1994; Paper I) applies one-dimensional clustering analysis to objects situated within a set of narrow cores samples (which may be either

conical or cylindrical). This one-dimensional clustering analysis is repeated for a series of sequentially decreasing core radii; the dependence of the mean free path between these clusters on the core radius allows us to discriminate between the filaments and the sheets intersecting the core sample. This ability to differentiate between filaments and sheets is based upon a simple geometrical model in which large coherent structures in the galaxy distribution are composed of a system of randomly distributed straight lines and flat planes. This method can be applied successfully to deep pencil beam redshift surveys and permits the measure of the mean free path between filaments and between sheets; it further allows rough estimates of other characteristics of the large-scale structure, such as the fraction of galaxies within each of these two populations. In tests with various simple point distributions, these measures are found to have large variances if such structures are not actually present (Buryak et al. 1994). Thus, the modest variances in the core sampling results from observational data themselves indicate the true existence of filamentary and sheet-like structures in the local Universe.

The 3D analyses described in the present paper, however, yield smoothly varying distribution functions having no dramatic features to suggest the presence of two or more distinct populations of structure. In particular, the more sophisticated 3D analyses would imply a smoothly varying continuum in the richness, the dimensionality, and the morphology of structure in the large-scale galaxy distribution.

This result does not necessarily contradict the results of Paper I, since core-sampling analysis will *by design* cleanly separate out two populations. In contrast, the present 3D analyses (MST and NCLL) do not try to impose an a priori geometry to the structure, but, instead, measure some aspects of the geometry directly. MST and NCLL nicely complement the core sampling analysis, providing, in particular, more direct probes of the morphology of the structure elements. Thus, the distribution functions discussed in Section 4 would indicate that the populations are not as distinct as the simpler core sampling analysis produces by design, but that there is rather a relatively smooth transition region where the properties (e.g. richness, dimensionality and morphology) of the richer filamentary structures may overlap those of the poorer sheet-like structures. Importantly, however, the analyses of Paper I and the analyses of this paper both agree that there exists a population of rich structure elements with a characteristic scale, $\sim 50 h^{-1}$ Mpc, and containing a representative fraction of galaxies (~ 40–50 per cent).

The methods and criteria of the 3D analyses and of the core-sampling approach are very different, and it is presently not possible to adequately identify the individual clusters in the 3D sample with the elements found by core-sampling. Naturally we expect that the filamentary and sheet-like components found with the core sampling approach are associated mostly with the poorer and with the richer clusters, respectively, which were discussed above. Indeed, the morphological analysis confirms that, for the LCRS, the filamentary type dominates for poorer structure elements, whereas the richer clusters are more sheet-like. On the other hand, it can be also shown that there exists a significant intermediate population which can be equally assigned to either filaments or sheets.

Bearing these comments in mind, we will now give more attention to the investigation of the internal properties and of the spatial distribution of the richer structure elements that can be found using the statistical methods described above.
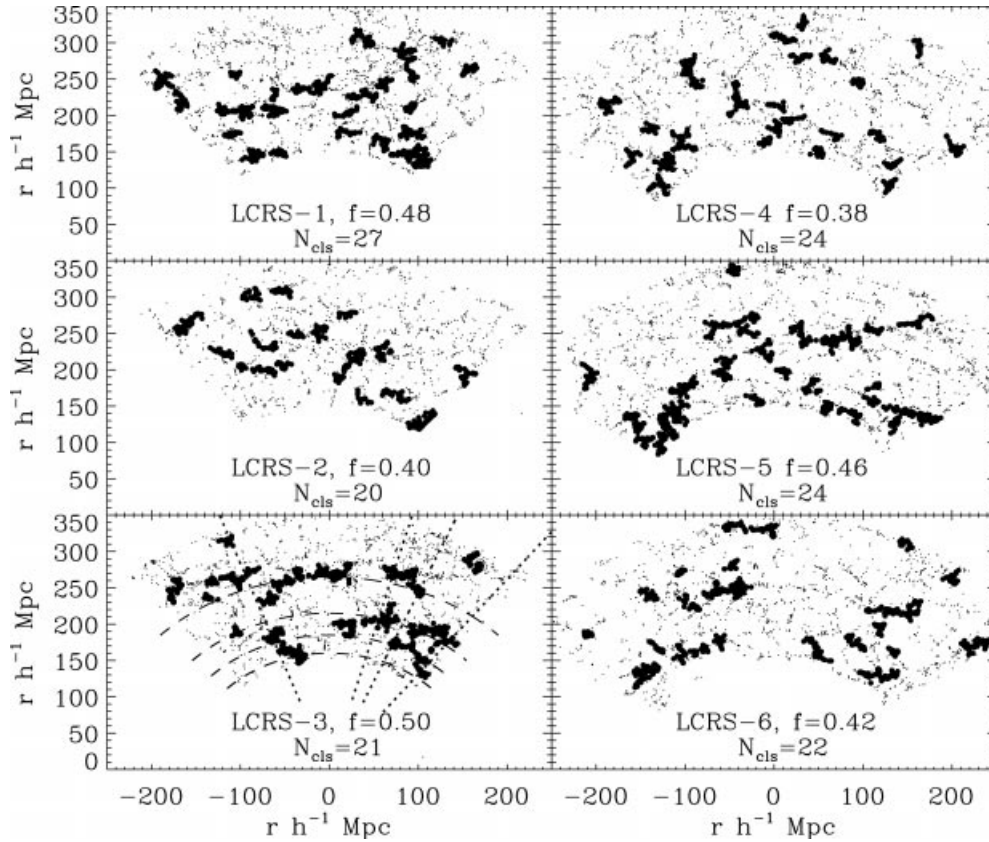
Figure 8. Spatial distribution of the richer clusters ($b_{thr} = 1.25$) for the LCRS-350 corrected for the selection effect. N_{cl} and f_{cl} are numbers of and fractions of galaxies in richer clusters. The galaxy number densities along the dotted and dashed lines (LCRS-3) are shown in Fig. 9.

5.1 Distinction of the richer structure elements

A sample of overdense regions can be extracted for each slice using the same range of linking lengths as above, $1 \leqslant b_{thr} \leqslant 1.3$. As before, two threshold linking lengths, $b_{thr} = 1$ and 1.25, were chosen for a more detailed study. These linking lengths correspond to a threshold overdensity bounding the clusters of $n_{thr}/\langle n_{gal}^{obs}\rangle = b^{-3} = 1$ and 0.5, respectively.

For the DURS (Doroshkevich et al. 2000) and for the simulated DM catalogues (DMRT) the value $b_{thr} \approx 1$ was found to be the most suitable. The larger value $b_{thr} \approx 1.25$ also used here allows us to compensate partly for the destruction of the observed structure caused by the small angular sizes of the LCRS slices and by the field-to-field sampling variations. Comparison of the LCRS with the available mock catalogues performed in Doroshkevich et al. (in preparation) allows one to reveal and to estimate the influence of slice thickness in more details.

The subsamples of richer clusters prepared for $b_{thr} = 1.25$ for the LCRS-350 and corrected for radial selection effects (as was described in Section 3.2) are plotted in Fig. 8. For all the slices $\sim$45 per cent of galaxies occupy $\sim$ 5–7 per cent of the slice volume at overdensities of about a factor of 7–10 above the mean. For the slice LCRS-3 this figure is similar to fig. 12 in Paper I. This figure shows that in all slices most of the richer clusters are actually situated at distances $D \leqslant 350\,h^{-1}$ Mpc. Direct test confirms that only 12–15 per cent of galaxies assigned to these clusters are situated at $D \geqslant 350\,h^{-1}$ Mpc and only for the slice LCRS-6 does this fraction increase to $\sim$30 per cent.

The galaxy distributions in the LCRS-3 slice along four radial

and four transverse lines are plotted in Fig. 9 (the positions of these lines are indicated in Fig. 8). Higher peaks correspond to the selected clusters. A similar 1D galaxy distribution was observed in deep pencil beam surveys (e.g. Broadhurst, Ellis & Shanks 1988; Broadhurst et al. 1990). The noticeable thickness of the peaks is caused by the random orientation between the lines and the large-scale structures they intersect.

For two linking lengths, $b_{thr} = 1$ and 1.25, subsamples of richer clusters were prepared for each of the six slices of the LCRS-350 so that the fraction of galaxies incorporated into clusters $f_{cl} \approx 0.45$. The mean proper parameters of these clusters are listed in Table 4. As before, averaging has been performed over all the clusters and each cluster was weighted by the *observed* number of cluster members N_{mem}. As before, the influence of selection effects on these cluster properties does not exceed $\sim$10 per cent, which demonstrates the effectiveness of the methods used for the cluster description.

N_{thr} and $\langle N_{mem}\rangle$ vary by about a factor of 2 from slice to slice. As was noted above these variations are proportional to the mean density of slices, and, as before, for the mean volume of clusters, $\langle V_{cl}\rangle$, defined by (4.1), we have

$$\langle V_{cl}\rangle = (5.7 \pm 0.5) \times 10^3\,h^{-3}\,\mathrm{Mpc}^3, \quad b_b = 1, \tag{5.1}$$

$$\langle V_{cl}\rangle = (9.5 \pm 2.1) \times 10^3\,h^{-3}\,\mathrm{Mpc}^3, \quad b_b = 1.25. \tag{5.2}$$

The slice-to-slice variations in the dimensionless proper parameters also do not exceed 20 per cent for $\langle \lambda \rangle$ and 10–12 per cent for the other characteristics. This high stability demonstrates the effectiveness of using dimensionless parametrizations to diminish
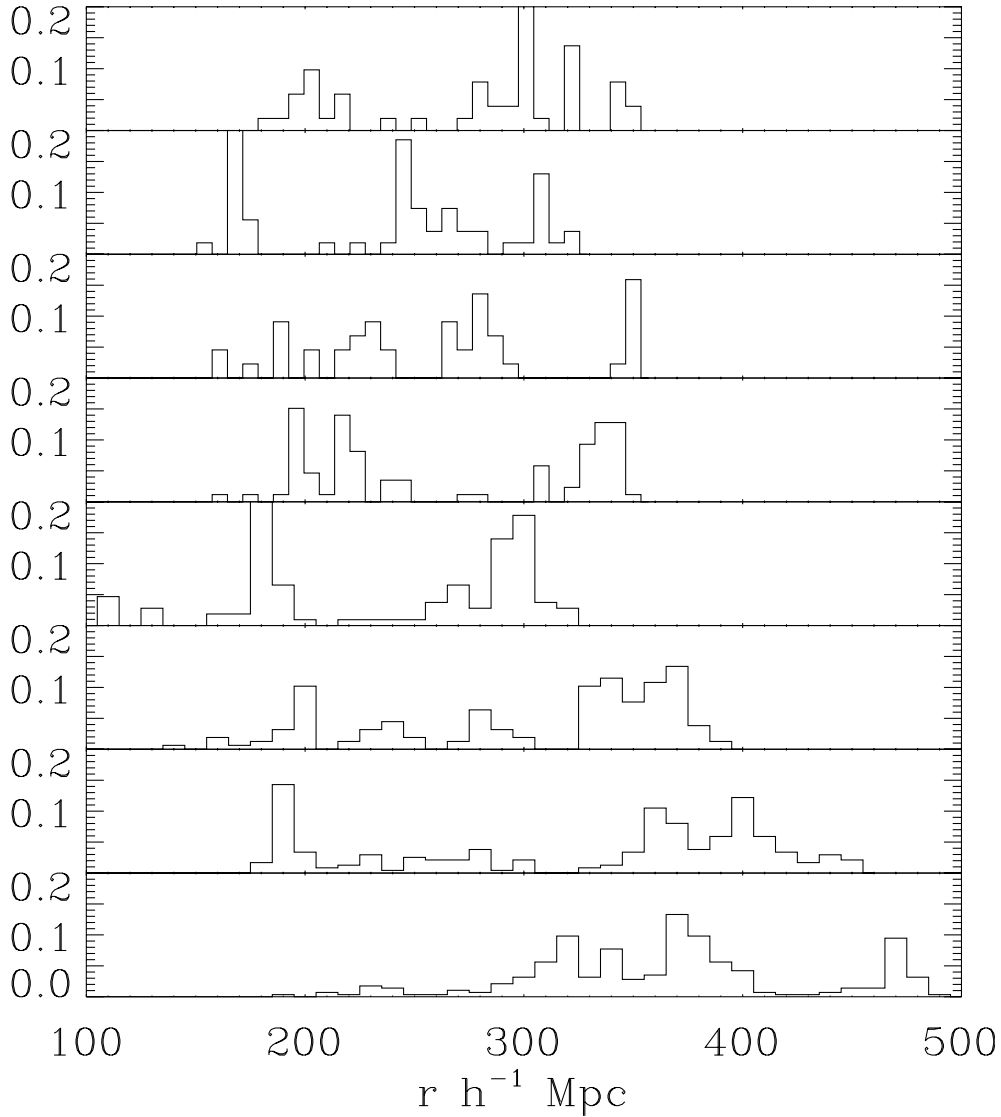
Figure 9. The galaxy number density in the LCRS-3 along four radial lines (four top panels, dotted lines in Fig. 8) and four transverse lines (four bottom panels, dashed lines in Fig. 8)

the consequences of slice-to-slice sampling variations and thereby to yield more objective measures of structure properties. All of these values are found to be similar to those listed in Table 3 for a broader sample of structure elements, thus confirming the smooth dependence of the mean properties of structure elements on richness N_{mem}, N_{thr} and linking length threshold b_{thr}.

The strong variations in the power indices, p_λ, p_ω, and especially p_θ – as compared with results listed in Table 3, results from the DURS (Doroshkevich et al. 2000), and results for DM simulations (DMRT) – are probably caused by the small angular size of slices, which restricts the growth of the measured wall thickness, θ, and increases the mass dependence of the two larger dimensions of the proper size. The degree of these distortions as well as of the distortions of proper sizes, $\langle\lambda\rangle$, $\langle\omega\rangle$, $\langle\theta\rangle$ and $\langle D_{prw}\rangle$, can be estimated by comparison with the DURS, which is not so afflicted, and with the DM simulations. For the DURS at $b_{thr} = 1$ these values have been found to be as follows:

$$\langle\lambda\rangle \approx (27 \pm 6)\, h^{-1}\, \text{Mpc}, \quad \langle\omega\rangle \approx (12 \pm 3.5)\, h^{-1}\, \text{Mpc},$$

$$\langle\theta\rangle \approx (6.5 \pm 3)\, h^{-1}\, \text{Mpc} \quad \langle D_{prw}\rangle = (26\, h^{-1} \pm 2.5)\, \text{Mpc}$$

$$p_\lambda \approx p_\omega \approx p_\theta \approx 0.5, \quad p_{prw} \approx 0.31. \tag{5.3}$$

For the simulated DM distribution for lower-density cosmological models these parameters at $b \approx 1$ have been found to have the following values:

$$\langle\lambda\rangle \approx (20 \pm 7)\, h^{-1}\, \text{Mpc}, \quad \langle\omega\rangle \approx (10 \pm 3)\, h^{-1}\, \text{Mpc}, \tag{5.4}$$

$$\langle\theta\rangle \approx (5.5 \pm 1.5)\, h^{-1}\, \text{Mpc}, \langle D_{prw}\rangle = (20\, h^{-1} \pm 2)\, h^{-1}\, \text{Mpc},$$

and all power indices in equation (4.8) are equal to 0.33. This comparison demonstrates that the influence of small slice thickness of the LCRS appears mainly in the distortion of the mass dependence of cluster thickness (4.8) and in the weak sensitivity of cluster parameters to the threshold linking length b_{thr}. The mass dependence of the proper sizes of proto-walls, described by (4.10) and (4.11) with $p_{prw} \approx 0.2$–0.3, is more similar to that found in Section 4.3 and for DURS and for DM simulations.

Comparison of $\langle\omega\rangle$, $\langle\theta\rangle$ and $\langle D_{prw}\rangle$, listed in Table 4 shows that for the LCRS, the formation of richer structure elements can be roughly described as an asymmetric 2D matter compression of a

factor of about 2 along the intermediate axis (width) and of a factor of about 4–6 along the smallest axis (thickness). The possible compression along the largest axis, L, is considered negligible. These estimates demonstrate that the observed walls are formed during *non-linear* matter compression over large scales (~ 20–$25\,h^{-1}\,\mathrm{Mpc}$).

The greatest matter compression is also observed in rich clusters of galaxies where the overdensity reaches factors of 10^3 or more. However, rich clusters of galaxies encompass only a relatively small fraction of all galaxies ($\leqslant 10$ per cent, Bahcall 1988), and, thus, their formation could merely be related to rare peculiarities in the initial density perturbations. In contrast, here we must deal with a much more representative fraction of galaxies (~ 40–50 per cent) which indicates that non-linear matter compression on such very large scales was typical over the observed course of structure evolution.

Theoretical analysis (Demiański & Doroshkevich 1999a,b) confirms that, for suitable parameters of cosmological models (OCDM and ΛCDM), the formation of such walls is a natural result of the evolution of initial perturbations with a CDM-like transfer function and a COBE-normalized Harrison–Zel'dovich primordial power spectrum.

5.2 The richest walls

The main characteristics of the richest walls in each slice are listed in Table 5. Random variations of these characteristics are enhanced by variations in the mean observed density of galaxies in the different slices. Extremely rich walls are found in the better-sampled LCRS-1, LCRS-3, LCRS-5 and LCRS-6 slices, whereas in the poorer-sampled LCRS-2 and LCRS-4 slices the characteristics of the largest walls are more modest. This difference confirms that the dimensional structure characteristics are sensitive to sampling effects and depend on the sample under investigation.

This effect is caused in part by the random orientation of walls relative to the thin LCRS slices and is amplified by the broken character of the walls themselves, which are composed of a system of filaments and denser clumps with typical separations of ~ 3–$5\,h^{-1}\,\mathrm{Mpc}$. Thus, for example, the proper characteristics of the richest walls in slices 3 and 5 in Table 5 differ by roughly a factor of 1.5–2 for the values of b_{thr} employed. A similarly complex intrinsic structure is clearly seen for the Great Wall in fig. 5 of Ramella et al. (1992). In the LCRS, the natural variations are reinforced by slice-to-slice and field-to-field variations in the sampling characteristics. Similar estimates obtained in other observed (DURS) and simulated catalogues (DMRT, CHWF) confirms the sensitivity of the parameters of the richest structure elements to the thresholds used and to the sample under investigation.

These results confirm the existence of very large walls having lengths up to ~ 50–$70\,h^{-1}\,\mathrm{Mpc}$. These sizes are comparable to the mean free path between the richer clusters to be discussed in the next section and in Paper I and to those obtained by Oort (1983a) and Ramella et al. (1992).

5.3 The mean free path between richer clusters

The typical separation of the wall-like structure elements (or, equivalently, the typical size of the underdense regions) is also an inmportant characteristic of the large-scale galaxy distribution. The broken character of the walls makes the definition of these

sizes uncertain and arbitrary. In fact, one can say that there is a single underdense region in the Universe and a system of high-density clumps situated within it. Thus, a variety of definitions for the typical size of these regions is possible and such estimates depend on both the definition and the sample under investigation. One such definition has been introduced by the core-sampling method and it results in a mean value for this size of $D_{\mathrm{s}} = 50$–$60\,h^{-1}\,\mathrm{Mpc}$ for the same LCRS sample depth (Paper I).

Now we can employ another definition of the typical size of underdense regions using the sample of richer clusters found above. Following the main ideas of the core-sampling approach, we will find the set of the separations for these clusters along a random straight line (the free path) both in the radial and in the transverse directions. The main advantage of such an approach is the use of the same given sample. The arbitrary character of such a definition of size is an inevitable consequence of the irregular shape and distribution of richer clusters.

To obtain such estimates, the sample of galaxies incorporated by the richer clusters (as described in Section 5.1) was divided into a system of conical cores with an angular diameter of $D_{\mathrm{core}} = 1°.5$, which is in accordance with the beam size of the LCRS, and again with an angular diameter of $D_{\mathrm{core}} = 1°.6$, which permits us to test the effects of random intersections between the cone and the walls. In each cone galaxies were collected into point-like clusters (with linking lengths appropriate to the b_{thr} for each slice) placed at each of their centres of mass. The set of separations for such points along the cones was used as a measure of the size of the underdense regions along a random radial straight line. To test the multi-intersection of the core with random boundaries of individual walls both the minimum multiplicity of the clusters, $N_{\mathrm{min}} = 1$, and a second multiplicity, $N_{\mathrm{min}} = 6$, were used. The same procedure was repeated for a set of cylindrical cores with diameter $D_{\mathrm{core}} = 10$ and $15\,h^{-1}\,\mathrm{Mpc}$ oriented along arcs of right ascension. The selection criteria and the method of sample preparation differ from those used in Paper I.

The mean separations of walls, $\langle D_{\mathrm{sep}} \rangle$, and their dispersions, σ_{sep}, are listed in Table 6, where N_{sep} is the number of separations found in the analysis for the accepted parameters. These results show that there is an essential number of random poorer clusters compiled by one to three galaxies, which decreases the measured wall separation for smaller N_{min}. Results obtained for larger N_{min} are in good agreement with those found in Paper I.

The distribution function of separations, $W(D_{\mathrm{sep}})$, is plotted in Fig. 10 for the same six versions together with exponential fits. It shows that in all cases there is a stable Poisson-like distribution of separations for $2.5\langle D_{\mathrm{sep}} \rangle \geqslant D_{\mathrm{sep}} \geqslant 0.5\langle D_{\mathrm{sep}} \rangle$. For $N_{\mathrm{min}} = 1$ there is a significant excess of smaller D_{sep} caused by random noise from poorer clusters.

5.4 Inner structure of the richer clusters and under-density regions

An important additional characteristic of the inner structure of the richer clusters and the filamentary component in underdense regions can be found with the NCLL and MST techniques as applied to the subsamples of such clusters and to the subsamples of underdense regions retained after a removal of richer clusters. With these methods we investigate the statistics of the point separations within these subsamples separately and can specify the properties of the large-scale galaxy distribution. The subsample of richer clusters prepared for $b_{\mathrm{thr}} = 1.25$ and plotted in Fig. 8 was employed for this investigation. The main results are plotted in

Table 6. Mean separation of the richer clusters.

D_{core}	N_{min}	N_{sep}	$\langle D_{sep}\rangle$	σ_{sep}
1°.5	1	384	38.6	33.0
1°.5	6	94	57.5	35.0
1°.6	6	94	55.2	35.0
$10\,h^{-1}$ Mpc	1	532	44.3	45.6
$10\,h^{-1}$ Mpc	6	181	78.3	54.8
$15\,h^{-1}$ Mpc	6	158	76.9	52.0
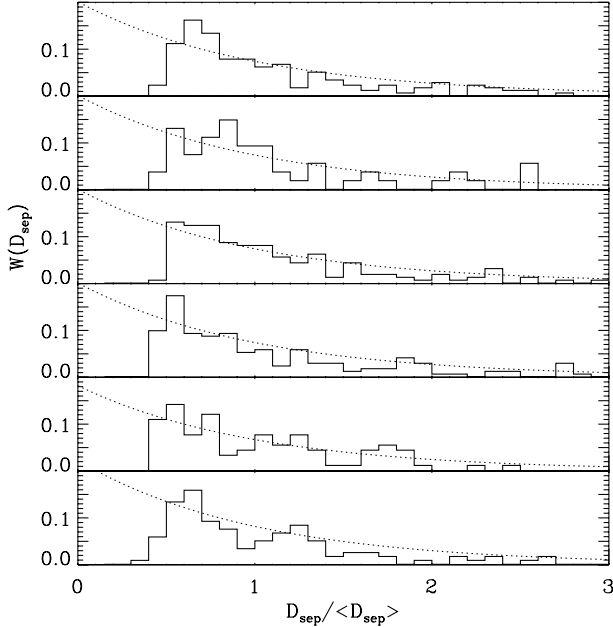
Figure 10. The distribution of the separation of richer clusters along the radial (three top panels) and transverse (three bottom panels) directions. Exponential fits are plotted by the dotted lines.

Fig. 11 and listed in Table 7 where $\langle\delta_{obs}\rangle$ is the mean overdensity with respect to the mean density of galaxies in a slice.

In Fig. 11 the PDF MSTs for the richer clusters in the six individual slices are plotted together with the PDF MST for the full sample of such clusters (top panel), prepared by averaging the individual PDF MST, $W_{MST}(l/\langle l_{MST}\rangle)$, over the six slices. The six-parameter fits (2.4) are also plotted in Fig. 11 for all PDF MSTs. It demonstrates the existence of a stable asymptotic $p_{MST} \approx 1.6$ at $l \geq \langle l_{MST}\rangle$, which differs significantly from the results obtained for the underdense regions. Averaging over slices results in the estimates

$$\langle p_{MST}\rangle = 1.6 \pm 0.2, \tag{5.5}$$

which is consistent with that listed in Table 7 for the full sample of richer clusters. The errors were obtained as described in Section 3.3.

For the underdense regions formed by the removal of richer clusters from the full slices, our results, obtained both with the NCLL and MST techniques, demonstrate the domination of filamentary structure formed by the less massive clumps and by individual galaxies. Averaging over the slices results in the estimates

$$\langle p_{MST}\rangle = 1.0 \pm 0.17. \tag{5.6}$$

Values for the power index $p_{cl}(b)$, obtained via the NCLL
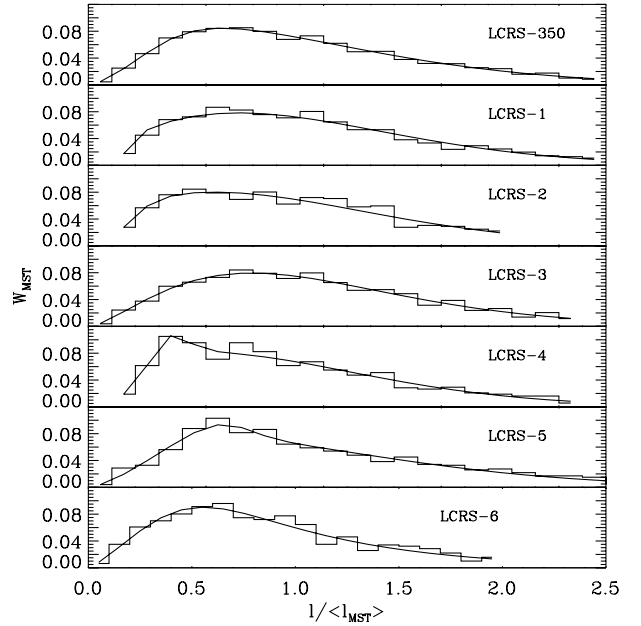
Figure 11. The PDF MSTs for the richer clusters in six slices of the LCRS-350 and for the full sample of such clusters (top panel). The best fits (2.4) are plotted by the solid line.

Table 7. Fit parameters for the richer clusters and under density regions from the six slices of the LCRS-350 sample plotted in Fig. 8 and for the full samples of richer clusters and underdense regions.

	$\langle\delta_{obs}\rangle$	$\langle l_{MST}\rangle$ h^{-1} Mpc	p_{MST}	p_{cl}
		Richer clusters		
LCRS-350	5.9	2.2	1.6 ± 0.09	1.7 ± 0.34
LCRS-1	6.5	2.0	1.7 ± 0.21	1.7 ± 0.24
LCRS-2	6.7	2.5	1.7 ± 0.23	1.8 ± 0.05
LCRS-3	4.7	1.8	1.7 ± 0.22	1.8 ± 0.04
LCRS-4	6.9	2.4	1.6 ± 0.07	1.5 ± 0.05
LCRS-5	5.4	2.1	1.6 ± 0.08	1.6 ± 0.15
LCRS-6	9.0	2.6	1.4 ± 0.27	1.5 ± 0.24
		Underdense regions		
LCRS-350	0.6	3.9	1.0 ± 0.07	1.0 ± 0.17
LCRS-1	0.6	3.5	1.1 ± 0.17	1.2 ± 0.09
LCRS-2	0.6	4.4	0.9 ± 0.25	0.8 ± 0.22
LCRS-3	0.6	3.6	1.0 ± 0.14	1.0 ± 0.11
LCRS-4	0.7	4.0	1.1 ± 0.17	1.1 ± 0.07
LCRS-5	0.6	3.9	1.0 ± 0.07	1.0 ± 0.04
LCRS-6	0.6	4.2	0.9 ± 0.19	1.0 ± 0.10

technique, are listed in Table 7 for larger $b \geq 1$ for the same samples. Within the range of errors they are consistent with results obtained by the MST approach.

Both the NCLL and PDF MST methods demonstrate the representative difference between the power indices obtained for larger b for the richer clusters and for the underdense regions. The power index varies slightly from slice to slice, which shows the diversity of the observed characteristics of the large-scale galaxy distribution.

6 CHARACTERISTICS OF THE FILAMENTARY COMPONENT

The filamentary component of the structure is formed by poorer clusters, and thus it is more sensitive to the selection effects

Table 8. Mean separation and surface density of filaments.

N_{min}	N_{sep}	$\langle D_{sep} \rangle$ h^{-1} Mpc	σ_{sep} h^{-1} Mpc	$10^3 \times \sigma_f$ h^2 Mpc^{-2}	D_f h^{-1} Mpc
		Radial core, $\theta_{core} = 1°\!.5$			
1	1913	17.0	12.6	5.8	13.2
2	1090	25.4	18.5	3.8	16.2
3	720	31.2	21.4	3.2	17.9
5	154	40.6	25.6	2.4	20.4
		Transversal core, $D_{core} = 10\, h^{-1}$ Mpc			
1	1476	15.1	10.7	6.4	12.5
2	874	23.1	18.2	3.7	16.4
3	632	28.9	22.0	3.4	17.1
5	334	38.0	24.0	2.6	19.8

discussed in Section 3. None the less, some of characteristics of this component can be found with the techniques used here.

A subsample of filaments can be prepared by the removal of the richer clusters from the full slices. As was discussed in Section 5.4, for this subsample $\langle p_{MST} \rangle \approx 1$, which points out the domination of a 1D galaxy distribution within the underdense regions. Analysis similar to that performed in Section 5.1 confirms this result. Thus, for the 526 clusters with a minimal richness $N_{min} = 5$ for $b_{thr} = 1$, we have

$$\langle N_{mem} \rangle = 8.0, \quad \langle \epsilon \rangle = 0.85, \quad \sigma_\epsilon = 0.1, \quad p_\epsilon = 0.22. \qquad (6.1)$$

As before, the distribution of ϵ is similar to Gaussian. Larger values of $\langle \epsilon \rangle$ relative to those listed for the richer structure elements in Table 4 confirms the filament-like character of the galaxy distribution within regions of lower density.

Proper sizes of filaments cannot be found with the inertia tensor technique owing to the many branches and the random shapes of filaments. The appropriate definition of the typical length of filaments, l_f, which applies to the network of filaments as well, is the distance between branch points along the trunk. However, even so defined, the length l_f depends upon the minimal richness of the branches included, N_{br}. With this definition, we have for the length of filaments

$$\langle l_f \rangle = 9.7, \quad \sigma_{l_f} = 4.1, \quad N_{br} = 3. \qquad (6.2)$$

For larger N_{br}, the value of l_f rapidly increases. The distribution of l_f is also found to be Gaussian-like, with a mean value and dispersion, σ_{l_f}, as given in (6.2).

A third characteristic of the filamentary component is the surface density of filaments, σ_f, which is the mean number of filaments intersecting a unit area of arbitrary orientation. Using the same method as in Section 5.3, we can measure the mean free path between filaments, but, in this case, the mean free path depends upon the physical size of the core sample, since the number of filaments crossing the core sample increases proportionally with the core sample's surface area. As was found in Paper I, the surface density of filaments and their measured mean free path, $\langle D_{sep} \rangle$, are linked by expressions

$$\sigma_f^{-1} = 0.25\pi\theta_{core}(D_{min} + D_{max})\langle D_{sep} \rangle,$$

$$\sigma_f^{-1} = 0.5\pi D_{core}\langle D_{sep} \rangle, \qquad (6.3)$$

for conical and cylindrical core samples, respectively. In these equations, D_{min} and D_{max} represent the minimal and maximal depths of the core sample, and θ_{core} and D_{core} represent the core sample's angular diameter (for conical core samples) and the linear diameter (for cylindrical core samples).

The analysis was performed for all slices of the LCRS-350 for $b_{thr} = 1$. As before, both a system of radial cores, $1°\!.5$ in diameter, and a system of cylindrical cores, $10\, h^{-1}$ Mpc in diameter and oriented along arcs of right ascension, were used. [Owing to the wedge geometry of the LCRS slices, the actual diameters of the cylindrical cores vary from $3.9\, h^{-1}$ Mpc at the minimum distance $D_{min} = 150$–$9.16\, h^{-1}$ Mpc at the maximum distance $D_{max} = 350\, h^{-1}$ Mpc. To correct the cylindrical core sample results for this effect, the mean diameter of core $D_{core} = 6.54\, h^{-1}$ Mpc at the mean distance $\langle D \rangle = 250\, h^{-1}$ Mpc was used in (6.3) to find σ_f.]

The main results are listed in Table 8, where N_{sep} and σ_{sep} are number and dispersion of the measured separations of filaments, and where $D_f = \sigma_f^{-1/2}$ is the mean separation of filaments independent of the size of the core sample used. The formal precision of these estimates – ~10 per cent – can be obtained by comparing results from individual slices, but their true reliability really depends upon the (unknown) influence of selection effects which destroy observed filaments more effectively than richer clusters.

As before, the distribution of measured separations is similar to an exponential, confirming the Poisson-like character of the cluster distribution along the core sample. The resulting estimates of the surface density of filaments, σ_f, obtained for both radial and transversal directions, are very similar to each other. For $N_{min} = 1$, they are also close to those obtained in Paper I for all filaments, $\sigma_f = (9.6 \pm 0.8) \times 10^{-3}\, h^2$ Mpc^{-2}, whereas for larger values of N_{min} ($N_{min} = 3$ and 5), they approach the value $\sigma_f = (1.4 \pm 0.3) \times 10^{-3}\, h^2$ Mpc^{-2} found in Paper I for the subpopulation of rich filaments. The value $D_f \approx 13\, h^{-1}$ Mpc obtained for the $N_{min} = 1$ is close to the mean length of filaments, $\langle l_f \rangle = 9.7\, h^{-1}$ Mpc, given by (6.2).

7 SUMMARY AND DISCUSSION

In this paper, we have used the opportunity of a large modern survey, the LCRS, as a basis for estimates of some of the physical and statistical properties of large-scale structure in the distribution of galaxies. We have conservatively used the best sampled part of the LCRS, restricting ourselves to the distance interval of $150 \leqslant D \leqslant 350\, h^{-1}$ Mpc, yielding a catalogue of 16 756 galaxies in the six LCRS slices. Paper I presented the results of applying the core-sampling analysis. Here, we apply a three-dimensional clustering analysis and the minimal spanning tree analysis. The survey is sufficiently deep and well sampled to provide for the first time a fairly representative sample of structure elements and, thus, reasonable estimates of structure properties.

First, we must mention a few cautionary notes.

(i) Our analysis uses redshift-space distances for galaxies. Thus, peculiar motions will tend to distort slightly our estimates of the proper sizes of the structure elements and other characteristics of the structure.

(ii) Although we have taken certain precautions against them (Section 3.2), residual effects of the field-to-field sampling variations and random galaxy selection inherent to the LCRS may still distort some of our estimates.

(iii) The proper sizes of the richer structure elements as well as the threshold parameters used are distorted by the finite angular thickness of the LCRS slices.

(iv) Our estimates of the parameters of the filamentary component are sensitive to the population of fainter galaxies, which may be undersampled by the LCRS. Although we briefly

report here for completeness our results for this population, our main concern in this paper is with the parameters of richer structure elements.

As noted before, the LCRS was clearly not planned with the NCLL and PDF MST methods in mind. Still, owing to its relative depth and number of galaxies, the LCRS is the best wide-field redshift survey presently available for such analyses. Therefore, the results presented here are by no means the final word on the properties of large-scale galaxy distribution; nevertheless, they do present a major step forward in our understanding of the large-scale distribution of galaxies. They can be used for comparison with similar parameters found for other observed and simulated catalogues (DURS, DMRT, CHWF), and with theoretical predictions (Demiański & Doroshkevich 1999a,b). The comparisons show that for most of the large-scale structure parameters we examine the LCRS already provides useful estimates.

7.1   Main characteristics of the structure

The main results of our analysis can be summarized as follows.

(i) Structure elements have been identified with clusters found using a dimensionless linking length $b = b_{thr} \approx 1$–1.25, which implies a local threshold density bounding the clusters of $n_{thr}/\langle n_{gal}^{obs} \rangle = b_{thr}^{-3} = 1$–0.5. In this case, the structure elements with a threshold richness $N_{thr} = 5$ encompass $\sim$70–80 per cent of the galaxies in the sample; there is also a component of single galaxies ($f_s \approx 0.1$–0.15 of all galaxies). Such an approach has enabled us to extract a representative sample of structure elements, to obtain a systematic statistical description of the large-scale galaxy distribution, and to establish the main characteristics of these structure elements.

(ii) At the same b_{thr}, a significant fraction of galaxies ($f_{cl} \sim 0.4$–0.5) is found to be incorporated within a moderate number of richer structure elements, or overdense regions, similar to nearby superclusters of galaxies. The typical length and width of these clusters are as large as 40–70 and 15–20 h^{-1} Mpc, respectively. The typical mean free path between these elements, i.e. the size of the underdense regions, is estimated to be $\langle D_{sep} \rangle \sim 50$–70 h^{-1} Mpc with a dispersion of $\sigma_{sep} \sim 35$–50 h^{-1} Mpc.

(iii) It has been shown that these richer elements could have been created through a two-dimensional non-linear compression of volume with a typical initial cross-sectional size of $\sim$25–30 h^{-1} Mpc. This scale is $\sim$5 times the observed correlation length for galaxies ($r_0 \approx 5$–7 h^{-1} Mpc).

(iv) Some characteristics of the filamentary-like structure elements – such as their typical length, $\langle l_f \rangle \approx 9.7 \, h^{-1}$ Mpc, and surface density, $\sigma_f \approx (2$–6$) \times 10^{-3} \, h^2 \, \mathrm{Mpc}^{-2}$ – are found in Section 6. All characteristics of this component are found to differ significantly from those of the richer structure elements.

(v) Our analysis with the NCLL and PDF MST techniques demonstrates the typical difference between the galaxy distribution within the overdense and the underdense regions. The latter are dominated by one-dimensional galaxy structures for $b > 1$, $l > \langle l_{MST} \rangle$, whereas the observed inner structure of the former is far from filamentary. In a comparison with the results from DURS, the distinction is clearer still, suggesting that the thin-slice geometry of the LCRS has affected the results for the morphological characteristic of richer clusters. However, in general, the smooth distribution of the properties, ranging from the emptiest regions to the richer clusters, implies that these clusters cannot be delineated in any exact sense. Thus, richer clusters appear

sheet-like and the galaxy structures in the underdense regions filamentary, but the morphology of the population of structure elements with an intermediate richness can be less easy, if not impossible, to resolve.

(vi) The shape of the PDF MST indicates that, for the LCRS, a slow onset of percolation is expected, and this expectation is confirmed directly for the range of linking lengths investigated. This result is caused by the high concentration of galaxies within a moderate number of richer clusters, and it is reinforced by the geometry of the LCRS (being a set of thin slices). For the more truly three-dimensional observed and simulated catalogues percolation restricts the acceptable interval of b_{thr} to $\lesssim$1.2 (DURS, DMRT).

7.2   The richer structure elements

Richer structure elements are clearly seen in the observed galaxy distribution as a moderate number of highly dense, rich galaxy concentrations. They contain a significant fraction of all galaxies, are well bounded, and are easily identified by cluster analysis. In spite of their large proper sizes they occupy a relatively small fraction of space and are separated by large regions of low galaxy concentration. These peculiarities allow us to portray these elements as tracing the major part, at least, of the skeleton of the large-scale structure in the Universe.

At the same time, the continuous nature of the distribution of structure element properties and their gradual variation with cluster richness and threshold linking length make a clear separation between these richer and the numerous set of poorer structure elements difficult. Still, it is none the less possible to make a rough discrimination between the overdense and the underdense regions. First, the former are clearly seen, via the core-sampling method, as sheet-like elements containing $\sim$50 per cent of all galaxies. The mean separation of these elements, $\sim$50–60 h^{-1} Mpc, exceeds the mean separation for the filamentary population by about a factor of 3–5. These two parameters – the morphology and the mean separation – can thus be used for a coarse, but certain, identification of this population. Furthermore, the characteristics of the MSTs constructed for the overdense and the underdense regions are also found to be clearly different (Section 5.4), even more so in a similar analysis for the more three-dimensional DURS, which thus provides qualitative support for the LCRS core sampling results.

The reason overdense regions are of particular interest is because they form a population having quite striking properties, making their origin one of the most interesting questions of modern cosmology. In particular, independent of the matter of discriminating between over and underdense regions, it is very important to establish that *non-linear* matter condensation appears to have taken place on unexpectedly large scales, $\sim$25–30 h^{-1} Mpc, and that it has embraced a significant fraction of matter. This scale of non-linearity exceeds the typical scale of the galaxy correlation function (~ 5–7 h^{-1} Mpc) by a factor of $\sim$5. The large fraction of galaxies incorporated in overdense regions emphasizes that they are representative of the general galaxy distribution, which makes this problem all the more fundamental.

Recent simulations (Cole et al. 1997; DMRT, CHWF) confirm that the evolution of small perturbations with a CDM-like power spectrum can result in non-linear matter condensation into such clusters for OCDM and ΛCDM models of low mean density, $\Omega_m h \sim 0.2$–0.4. Other models tested – in particular, the SCDM

model with $\Omega_m = 1$ – cannot reproduce walls with the properties observed in the LCRS. These restrictions of cosmological parameters are consistent with those obtained by Bahcall & Fan (1998) and Perlmutter et al. (1999).

A theoretical analysis, as opposed to the numerical analysis of *N*-body simulations, would provide a physical understanding of the formation of structure. It is now a matter of history that, fundamentally, gravitational instability leads initially to the formation of Zel'dovich pancakes (Zel'dovich 1970). More recently, Demiański & Doroshkevich (1999b) have applied the Zel'dovich approximation to a CDM-like power spectrum to show that non-linear matter condensation does indeed take place on a scale similar to that found above; they connect this scale with the parameters of the power spectrum and cosmological models such as the velocity coherent length.

Interestingly, not only does collapse take place first along the shortest principal axis of a generally asymmetric density inhomogeneity, but transversal collapse soon follows. This gives rise to a filamentary region of high density contrast within a pancake, so that filamentary structure is 'seen' to dominate during the earlier evolutionary stages. Later on, many of the filaments are successively accumulated within sheet-like structures owing to merging and so form the subpopulation of richer structure elements. The Great Wall is such an example, as can be seen from a face-on picture of it (fig. 5 of Ramella et al. 1992). Within the now extended underdense regions, the remaining fraction of filaments and poorer pancakes continue to survive, thus forming the low end of the mass function. The epoch and degree of such a transformation will depend on the basic parameters of the cosmological model and power spectrum used. Thus, our observational results here and in Paper I would seem to imply that we are presently living in a particular intermediate epoch of structure evolution, when the population of 'Great Wall'-like structures contains a significant fraction of matter, yet with a smooth spectrum of structure, ranging from clear rich sheet-like walls to poor filaments.

7.3 General discussion

The richer clusters described above can also be compared with similar structures from other investigations. For instance, the nine superclusters compiled by Oort (1983a,b) have a longest dimension of 20–$75\,h^{-1}$ Mpc, an axial ratio of $\approx 6:1$ and a velocity dispersion of ~ 300–$400\,\mathrm{km\,s^{-1}}$, which corresponds (approximately) to a thickness for superclusters of ~ 6–$8\,h^{-1}$ Mpc. As a rule, a supercluster will contain several clusters of galaxies. One of these superclusters was later reclassified by de Lapparent et al. (1988) as the Great Wall, for which Ramella et al. (1992) estimated a length of $\sim 100\,h^{-1}$ Mpc and a thickness of $\sim 5\,h^{-1}$ Mpc. Similar parameters were also found for the Pisces–Perseus supercluster (Giovanelli & Haynes 1993). All these estimates are consistent with our estimates of the major parameters of richer clusters in the LCRS.

Of course, the scale ~ 20–$40\,h^{-1}$ Mpc and more has been described for over ten years as typical for the spatial distribution of rich clusters of galaxies (see, for example, Bahcall 1988). However, such clusters of galaxies form a peculiar population that incorporates only 5–10 per cent of galaxies. What we now see is that these same scales are typical for the population of richer clusters that incorporates a much greater fraction, ~ 50 per cent, of galaxies.

The galaxy distribution has also been studied with deep pencil beam surveys (Broadhurst et al. 1990; Willmer et al. 1994; Buryak et al. 1994; Bellanger & de Lapparent 1995; Cohen et al. 1996), where the typical size of underdense regions was found to be 60–$120\,h^{-1}$ Mpc with a velocity dispersion within the peaks of 400–$650\,\mathrm{km\,s^{-1}}$, corresponding to a typical thickness of about 8–$13\,h^{-1}$ Mpc. For such surveys the interpretation of the peaks is uncertain and only the thickness of elements along the line of sight can be found. These problems were discussed in detail in Paper I. There is also some observational evidence for strong inhomogeneities of the Universe at redshifts of $z \sim 0.5$–1 and more (Williger et al. 1996; Cristiani et al. 1997; Quashnock, Vanden Berk & York 1996, 1998; Connolly et al. 1996). These results show that the richer wall-like condensations are visible at least to a redshift of $z \approx 1$.

Similar 'superlarge' scales are typical in theoretical discussions of the scale of perturbations in the gravitational potential (for more detail, see Buryak, Demiański & Doroshkevich 1992; Sahni, Sathyaprakash & Shandarin 1994; Doroshkevich et al. 1997; Madsen et al. 1998; Demiański & Doroshkevich 1999a). In principle, such perturbations can, among other things, explain the observed quasi-regular character of the richer clusters. In this case, their formation can be described as matter infall into deep gravitational wells, while their unexpectedly large separation can be linked to a typical scale of the spatial distribution of deeper potential wells. One could then adopt another approach and study the problem of 'void' formation, as was done by Blumenthal et al. (1992) and by Piran et al. (1993). However, their definition of 'voids' differs from ours and, consequently, their estimates of possible 'void' sizes, as well as the 'void' sizes found recently by El-Ad, Piran & da Costa (1996), are related to the moderately rich structure elements rather than the separation of wall-like condensations.

Other possible factors can also essentially influence the observed galaxy distributions. For example, the probable large-scale bias between the galaxy and dark matter distributions (Rees 1985; Dekel & Silk 1986; Dekel & Rees 1987) may be essential for resolving this problem. In this case, both the typical size of protowalls and the fraction of dark matter within the observed richer clusters can be less than the values that were found above. For suitable parameters of the power spectra, such a bias can appear owing to the reheating of the baryonic component, which would need to occur at a redshift, $z \gtrsim 10$ (for more details see, for example, Dekel & Silk 1986; Dekel & Rees 1987; Buryak et al. 1992; Bower et al. 1993; Sahni et al. 1994; Fong, Doroshkevich & Turchaninov; Demiański & Doroshkevich 1999a,b; DMRT; Lee & Shandarin 1998).

Observationally, there clearly exists such a large-scale bias between the galaxy distribution and the baryonic component of the Universe. This is most simply seen by noting that the maximum ratio of luminous-to-gaseous baryonic fractions within clusters of galaxies is $\rho_{gal}/\rho_{gas} \sim 0.2$ (White, Briel & Henry 1993), whereas $\rho_{gal}/\rho_{gas} \ll 1$ in the Böotes void (Weistrop et al. 1992). Furthermore, the redshift distribution of Lyman-α absorbers in the spectra of quasi-stellar objects (QSOs) show a much more homogeneous spatial distribution of baryons in the intergalactic medium and, thus, also of dark matter. These large-scale modulations of ρ_{gal}/ρ_{gas} clearly constitute a large-scale bias.

In conclusion, our analyses show that richer wall-like structure elements, with their extraordinary large linear extents which yet occupy such a relatively small volume of space, contain about half of all galaxies and, thus, are the major component of large-scale structure in the Universe. This has lead to theoretical

investigations that show that they have generally formed through gravitational instability causing the two-dimensional collapse of density inhomogeneities. However, similar analyses of *N*-body simulations show that, to obtain their properties similar to those observed and the low velocity dispersions of the surprisingly cool Universe we seem to inhabit, not only is a low matter density, $\Omega_m h \sim 0.2$–0.3, implied, but also the need for the large-scale biasing of galaxies with respect to the dark matter in the Universe, be it solely baryonic or both baryonic and exotic dark matter (DMRT, CHWF). Clearly, the richness and wealth of the physical characteristics our analyses are able to explore make them potentially very useful methods for the analysis and interpretation in the new millennium of the very large surveys – such as the 2dF Galaxy Redshift Survey and Sloan Digital Sky Survey – which are now underway.

ACKNOWLEDGMENTS

REFERENCES

Babul A., Starkman G. D., 1992, ApJ, 401, 28
Bahcall N. A., 1988, ARA&A, 26, 631
Bahcall N. A., Fan X., 1998, ApJ, 504, 1
Barrow J., Bhavsar S., Sonoda D., 1985, MNRAS, 216, 17
Baugh C. M., Efstathiou G., 1993, MNRAS, 265, 145
Bellanger C., de Lapparent V., 1995, ApJ, 455, L103
Bhavsar S. P., Ling E. N., 1988, ApJ, 331, L63
Blumenthal G. R. et al., 1992, ApJ, 388, 234
Borgani S., 1996, in Bonometto S., Primack J., Provenzale A., eds, Dark Matter in the Universe
Bower R. G., Coles P., Frenk C. S., White S. D. M., 1993, ApJ, 405, 403
Broadhurst T. J., Ellis R. S., Shanks T., 1988, MNRAS, 235, 827
Broadhurst T. J., Ellis R. S., Koo D. C., Szalay A. S., 1990, Nat, 343, 726
Buryak O., Doroshkevich A., 1996, A&A, 306, 1
Buryak O., Demiański M., Doroshkevich A., 1991, ApJ, 383, 41
Buryak O., Demiański M., Doroshkevich A., 1992, ApJ, 393, 464
Buryak O. E., Doroshkevich A. G., Fong R., 1994, ApJ, 434, 24
Cohen J. G., Hogg D. W., Pahre M. A., Blandford R., 1996, ApJ, 462, L9
Cole S., Weinberg D. H., Frenk C. S., Ratra B., 1997, MNRAS, 289, 37
Cole S., Hatton S., Weinberg D. H., Frenk C. S., 1998, MNRAS, in press (CHWF)
Colless M. M., 1999, in Morgani R., Couch W. J., eds, Proc. ESO/Australia Workshop, Looking Deep in the Soutern Sky. Springer, Berlin, p. 9
Connolly A. J. et al., 1996, ApJ, 473, L67
Cristiani S. et al., 1997, MNRAS, 285, 209
da Costa L. N. et al., 1988, ApJ, 327, 544
de Lapparent V., Geller M. J., Huchra J. P., 1988, ApJ, 332, 44
Dekel A., Silk J., 1986, ApJ, 303, 39
Dekel A., Rees M. J., 1987, Nat, 326, 455
Demiański M., Doroshkevich A., 1999a, ApJ, 512, 527
Demiański M., Doroshkevich A., 1999b, MNRAS, 306, 779

Doroshkevich A. G. et al., 1996, MNRAS, 283, 1281 (Paper I)
Doroshkevich A. G. et al., 1997, MNRAS, 284, 633
Doroshkevich A. G., Fong R., Tucker D., Lin H., 1998, in Olinto A. V., Frieman J. A., Schramm D. N., eds, Eighteenth Texas Symposium on Relativistic Astrophysics and Cosmology. World Scientific, Singapore, p. 560
Doroshkevich A. G., Müller V., Retzlaff J., Turchaninov V. I., 1999, MNRAS, 306, 575 (DMRT)
Doroshkevich A. et al., 2000, MNRAS, 315, 767
Doroshkevich A. G., Fong R., Tucker D., Turchaninov V. I., 2001, MNRAS, in preparation
Dressler A. et al., 1987, ApJ, 313, L37
El-Ad H., Piran T., da Costa L. N., 1996, ApJ, 462, L13
Fong R., Doroshkevich A., Turchaninov V., 1995, in Holt S., Bennett C., eds, Dark Matter. Am. Inst. Phys., New York, p. 429
Huchra J. P., Geller M. J., 1982, ApJ, 257, 423
Giovanelli R., Haynes M. P., 1993, AJ, 105, 1271
Kendall M., Moran P., 1963, Geometrical Probability. Griffin, London
Kirshner R. P., Oemler A. J., Schechter P. L., Shectman S. A., 1983, AJ, 88, 1285
Kruskal J. B., 1956, Proc. Am. Math. Soc., 7, 48
Lee J., Shandarin S. F., 1998, ApJ, 505, L75
Lin H. et al., 1996, ApJ, 464, 60
Landy S. D. et al., 1996, ApJ, 456, L1
Loveday J., Pier J., 1998, in Colombi S., Mellier Y., Raban B., eds, Wide Field Surveys in Cosmology. Editions Frontières, Paris, p. 317
Madsen S., Doroshkevich A., Gottlöber S., Müller V., 1998, A&A, 329, 1
Martinez V. J., Jones B. J. T., Dominguez-Tenreiro R., van de Weygaert R., 1990, ApJ, 357, 50
Oort J. H., 1983a, ARA&A, 21, 373
Oort J. H., 1983b, A&A, 139, 211
Perlmutter S. et al., 1999, ApJ, 517, 565
Piran T. et al., 1993, MNRAS, 265, 681
Prim R. C., 1957, Bell. System Tech. J., 36, 1389
Quashnock J. M., Vanden Berk D. E., York D. G., 1996, ApJ, 472, L69
Quashnock J. M., Vanden Berk D. E., York D. G., 1998, in Olinto A. V., Frieman J. A., Schramm D. N., eds, Eighteenth Texas Symposium on Relativistic Astrophysics and Cosmology. World Scientific, Singapore, p. 655
Ramella M., Geller M. J., Huchra J. P., 1992, ApJ, 384, 396
Ratcliffe A. et al., 1996, MNRAS, 281, L47
Rees M. J., 1985, MNRAS, 213, 75ᴘ
Sahni V., Sathyaprakash B. S., Shandarin S. F., 1994, ApJ, 431, 20
Sahni V., Coles P., 1995, Phys. Rep., 262, 1
Sathyaprakash B. S., Sahni V., Shandarin S. F., 1998, ApJ, 508, 551
Shandarin S., Yess C., 1998, ApJ, 505, 12
Shectman S. A. et al., 1996, ApJ, 470, 172
Tucker D. L. et al., 1997, MNRAS, 285, L5
van de Weygaert R., 1991, PhD thesis, Univ. Leiden
Vishniac E. T., 1986, in Kolb E. W., Turner M. S., Lindley D., Olive K., Seckel D., eds, Inner Space/Outer Space. Univ. Chicago Press, Chicago, p. 190
Weistrop D. et al., 1992, ApJ, 396, L23
White S. D. M., 1979, MNRAS, 186, 145
White S. D. M., Briel U. G., Henry J. P., 1993, MNRAS, 261, L8
Williger G. M., Hazard C., Baldwin J. A., McMahon R. G., 1996, ApJS, 104, 145
Willmer C. N. A., Koo D. C., Szalay A. S., Kurtz M. J., 1994, ApJ, 437, 560
Zel'dovich Ya. B., 1970, A&A, 5, 20

This paper has been typeset from a TₑX/LᴬTₑX file prepared by the author.